

MODELLING MHD ACCRETION-EJECTION - FROM THE LAUNCHING AREA TO PROPAGATION SCALES

DENISS STEPANOV, CHRISTIAN FENDT

Max Planck Institute for Astronomy, Königstuhl 17, D-69117 Heidelberg, Germany

Draft version July 14, 2014

ABSTRACT

We present results of axisymmetric magnetohydrodynamic (MHD) simulations investigating the launching of jets and outflows from a magnetically diffusive accretion disk. The time evolution of the disk structure is self-consistently taken into account. In contrast to previous works we have applied *spherical* coordinates for the numerical grid, implying substantial benefits concerning the numerical resolution and the stability of the simulation. Thanks to the new setup we were able to run simulations for more than 150,000 dynamical times on a domain extending 1500 inner disk radii with a resolution of up to 24 cells per disk height in the inner disk. Depending on the disk magnetization, jet launching occurs in two different but complementary regimes - jets driven predominantly by centrifugal or magnetic forces. These regimes differ in the ejection efficiency concerning mass, energy and angular momentum. We show that it is the *actual* disk magnetization and not so much the initial magnetization which describes the disk-jet evolution best. Considering the actual disk magnetization we also find that simulations starting with different initial magnetization evolve in a similar - typical - way as due to advection and diffusion the magnetic flux in the disk evolves in time. Exploring a new, modified diffusivity model we confirm the self-similar structure of the global jet-launching disk, obtaining power laws for the radial profiles of the disk physical variables such as density, magnetic field strength, or accretion velocity.

Subject headings: accretion, accretion disks – MHD – ISM: jets and outflows – stars: mass loss – stars: pre-main sequence galaxies: jets

1. INTRODUCTION

Astrophysical jets as highly collimated beams of high velocity material and outflows of less degree of collimation and lower speed are an ubiquitous phenomenon in a variety of astrophysical sources. The role of magnetic fields in the realm of jets and accretion disks cannot be underestimated. It is crucial for the launching, acceleration, and collimation of jets (see, e.g. Blandford & Payne 1982; Pudritz & Norman 1983; Pelletier & Pudritz 1992; Camenzind 1990; Sauty & Tsinganos 1994; Pudritz et al. 2007). However, due to the complexity of the physical problem, the exact time evolution and geometry of these processes is still under debate.

Jets and outflows from young stellar objects (YSO) and active galactic nuclei (AGN) clearly affect their environment, and, thus, at the same time the formation process of the objects that are launching them (see, e.g., Banerjee et al. 2007; Gaibler et al. 2012). However, in order to quantify the feedback phenomenon - namely to specify how much mass, angular momentum, and energy is being ejected into the surrounding via the outflow channel - it is essential to model the physics in the innermost launching area of the disk-jet system with a high resolution. It is commonly accepted that ejection and accretion are tightly connected to each other (Li 1995; Ferreira & Pelletier 1995). The study of these phenomena is motivated also by the observed correlation between accretion and ejection signatures (Cabrit et al. 1990).

Our paper deals exactly with these topics - we will provide a relation between actual magnetization within the disk, and the ejection to accretion ratio for mass and energy.

The first numerical simulations of this kind were presented by Casse & Keppens (2002, 2004), who demonstrated how an outflow can be self-consistently launched out of the accretion disk, accelerated to high velocity and collimated in a narrow beam. Later Meliani et al. (2006) studied in particular the impact of a central stellar wind on the accretion disk magnetic field inclination. The work by Zanni et al. (2007) revealed the great importance of the underlying disk diffusivity, namely the strength of diffusivity and its directional anisotropy. Studying two limits of rather high and low diffusivity, and keeping the same (about equipartition) magnetic field strength and field structure, the authors found that a steady state of the simulation could not be reached for an arbitrary combination of these parameters. Tzeferacos et al. (2009) in particular found that the efficiency of the launching mechanism is strongly dependent on the disk magnetization.

A common assumption was that in order to launch jets, the magnetic field should be rather strong, somewhat about the equipartition value. This question was investigated in detail by Murphy et al. (2010), demonstrating that even with a weak magnetization of $\mu \approx 0.002$ jets could be driven.

So far, the general mechanism of jet launching from magnetized disks have been studied by a number of authors. However, due to the complexity of the problem, the combined action of the various processes engaged could not be easily disentangled. Another problem arises if only a short-term evolution of the system is considered, as this will be strongly dependent on the initial conditions. What is somewhat complicating the interpretation of simulations in the literature is that usually the model setup is categorized by the *initial* parameters, and not

by the *actual* quantities such as the actual disk magnetization, accretion velocity etc. at a certain evolutionary time. The latter was first discussed by Sheikhezami et al. (2012), however, the parameter space applied in those simulations was rather limited. In the present study we will show that it is the actual disk properties, in particular the disk magnetization, that govern the accretion and ejection.

Accretion disks are considered to be highly turbulent for any degree of the disk magnetization. The source of the turbulence is still debated, however, a great variety of unstable modes in magnetized accretion disks exists (Keppens et al. 2002). In case of moderately magnetized disks, the main candidate is the magneto-rotational instability (MRI) (Balbus & Hawley 1991; Fromang 2013). Highly magnetized disks are subject to the Parker instability (Gressel 2010; Johansen & Levin 2008) and the trans-slow Alfvén continuum modes (Goedbloed et al. 2004). The puzzling question is what is the effective diffusivity and viscosity the disk turbulence provides, and how can these effects be properly implemented under the mean field approach.

As shown by Hawley et al. (1995) and later adapted by Casse & Keppens (2004); Meliani et al. (2006), the turbulent energy and angular momentum flux is dominated by the magnetic stress rather than the Reynolds stress. Thus, in the presence of a moderately strong magnetic field the Reynolds stress becomes less important. In order to disentangle the complex behaviour and keep the simulations more simple, we explore only non-viscous disks.

Considering the accretion-ejection scenario, we are convinced that before any general relation between physical quantities can be claimed, it is essential that the system itself has dynamically evolved over a sufficiently extended period of time. We have therefore evolved our simulations for at least 10.000 dynamical times. We will show that such a long simulation requires that the advective and diffusive processes have to be well in balance.

In our paper we apply the following approach. First, we consider the standard diffusivity model (see e.g. Zanni et al. 2007). After having obtained a near equilibrium solution with advection and diffusion in balance, we closely examine the state of the system. Essentially, we will argue that it is the balance between diffusion and advection that governs the strength of the *actual* disk magnetization. The latter appears to be the key ingredient for the evolution of the whole system. Exploring a wide range of the actual disk magnetization allows us to derive a general correlation between the actual disk magnetization and major quantities of the disk-jet system, such as the mass and energy ejection efficiencies.

We also present a model setup which is well suited for a long-term evolution study of the jet launching problem. The use of spherical geometry provides a high resolution in the inner region of the disk - the site of jet launching, and a low resolution for the outer regions, where the physical processes typically evolve on much longer time scales.

Our paper is organized as follows. Section 2 describes the numerical setup, the initial and boundary conditions of our simulations. In Section 3 we discuss our reference simulation, that is characterized by the balance between advection and diffusion, and uses the standard diffusiv-

ity model. In Section 4 we present a detailed analysis of jet launching disks, revealing the major role of the disk magnetization in the disk-jet evolution. In Section 5 we discuss simulations applying a new diffusivity model that essentially overcomes the accretion instability observed in the previous simulations. This allows us to follow substantially longer the evolution of the disk-jet system. Finally we summarize our results in Section 6

2. MODEL APPROACH

We apply the MHD code PLUTO (Mignone et al. 2007), version 4.0, solving the time-dependent, resistive MHD equations on a spherical grid (R, Θ) . We refer to (r, z) as cylindrical coordinates. The code numerically solves the equations for the mass conservation,

$$\frac{\partial \rho}{\partial t} + \nabla \cdot (\rho \mathbf{V}) = 0, \quad (1)$$

with the plasma density ρ and flow velocity \mathbf{V} , the momentum conservation,

$$\frac{\partial \rho \mathbf{V}}{\partial t} + \nabla \cdot \left[\rho \mathbf{V} \mathbf{V} + \left(P + \frac{\mathbf{B} \cdot \mathbf{B}}{2} \right) \mathbf{I} - \mathbf{B} \mathbf{B} \right] + \rho \nabla \Phi_g = 0 \quad (2)$$

with the thermal pressure P and the magnetic field \mathbf{B} . The central object of point mass M has a gravitational potential $\Phi_g = -GM/R$. Note that equations are written in non-dimensional form, and as usual the factor 4π is neglected. We apply a polytropic equation of state, $P \propto \rho^\gamma$, with the polytropic index $\gamma = 5/3$.

The code further solves for the conservation of energy,

$$\frac{\partial e}{\partial t} + \nabla \cdot \left[\left(e + P + \frac{\mathbf{B} \cdot \mathbf{B}}{2} \right) \mathbf{V} - (\mathbf{V} \cdot \mathbf{B}) \mathbf{B} + \bar{\eta} \mathbf{J} \times \mathbf{B} \right] = -\Lambda_{\text{cool}}, \quad (3)$$

with the total energy density,

$$e = \frac{P}{\gamma - 1} + \frac{\rho \mathbf{V} \cdot \mathbf{V}}{2} + \frac{\mathbf{B} \cdot \mathbf{B}}{2} + \rho \Phi_g, \quad (4)$$

given by the sum of thermal, kinetic, magnetic, and gravitational energy, respectively. The electric current density is denoted by $\mathbf{J} = \nabla \times \mathbf{B}$. As shown by Tzeferacos et al. (2013), cooling may indeed play a role for jet launching, influencing both jet density and velocity. For the sake of simplicity we set the cooling term equal to Ohmic heating, $\Lambda_{\text{cool}} = -\bar{\eta} \mathbf{J} \cdot \mathbf{J}$. Thus all generated heat is instantly radiated away.

The magnetic field evolution is governed by the induction equation

$$\frac{\partial \mathbf{B}}{\partial t} = \nabla \times (\mathbf{V} \times \mathbf{B} - \bar{\eta} \mathbf{J}), \quad (5)$$

Our simulations are performed in 2D axisymmetry applying spherical coordinates. We use the Harten-Lax-van Leer (HLL) Riemann solver together with a third-order Runge-Kutta scheme for time evolution and the PPM (piecewise parabolic method) reconstruction of (Colella & Woodward 1984) for spatial integration. The magnetic field evolution follows the method of Constrained Transport (Londrillo & del Zanna 2004).

2.1. Numerical grid and normalization

Table 1

Typical parameter scales for different sources. Simulation results will be given in code units and can be scaled for astrophysical application.

	YSO	BD	AGN	[unit]
R_0	0.1	0.01	20	AU
M_0	1	0.05	10^8	M_\odot
ρ_0	10^{-10}	10^{-13}	10^{-12}	g cm^{-3}
V_0	94	66	6.7×10^4	km s^{-1}
B_0	15	0.5	1000	G
T_0	1.7	0.25	0.5	days
\dot{M}_0	3×10^{-5}	2×10^{-10}	10	$M_\odot \text{ yr}^{-1}$
\dot{J}_0	3.0×10^{36}	1.5×10^{30}	3×10^{51}	dyne cm
\dot{E}_0	1.9×10^{35}	6.7×10^{29}	2.6×10^{46}	erg s^{-1}

No physical scales are introduced in the equations above. The results of our simulations will be presented in non-dimensional units. We normalize all variables, namely $P, \rho, \mathbf{V}, \mathbf{B}$, to their values at the inner disk radius R_0 . Lengths are given in units of R_0 , corresponding to inner disk radius. Velocities are given in units of $V_{K,0}$, corresponding to the Keplerian speed at R_0 . Thus $2\pi T$ corresponds to one revolution at the inner disk radius. Densities are given in units of ρ_0 , corresponding to R_0 . Pressure is measured in $P_0 = \epsilon^2 \rho_0 V_0^2$.

We thus may apply our scale-free simulations to a variety of jet sources. In the following we show the physical scaling concerning three different object classes - brown dwarfs (BD), young stellar objects (YSO), and active galactic nuclei (AGN). In order to properly scale the simulations, we vary the following masses for the central object, $M = 0.05 M_\odot$ (BD), $M = 1 M_\odot$ (YSO), $M = 10^8 M_\odot$ (AGN), and, thus, define a scale for the inner disk radius of

$$\begin{aligned} R_0 &= 0.1 \text{ AU} \quad (\text{YSO}) \\ &= 0.01 \text{ AU} \quad (\text{BD}) \\ &= 20 \text{ AU} \left(\frac{R_0}{10 R_S} \right) \left(\frac{M}{10^8 M_\odot} \right) \quad (\text{AGN}), \end{aligned} \quad (6)$$

where $R_S = 2GM/c^2$ is the Schwarzschild radius of the central black hole. For consistency with our non-relativistic approach, we require $R_0 > 10 R_S$, implying that we cannot treat highly relativistic outflows. Table 1 summarizes the typical scales for leading physical variables. For more detailed scaling laws we refer to the Appendix A.

We apply a numerical grid with equidistant spacing in θ -direction, but stretched cell sizes in radial direction, considering $\Delta R = R \Delta \theta$. Our computational domain of a size $R = [1, 1500 R_0], \theta = [0, \pi/2]$ is discretized with $(N_R \times N_\theta)$ grid cells. We use a general resolution of $N_\theta = 128$. In order to cover a factor 1500 in radius, we apply $N_R = 600$. This gives a resolution of 16 cells per disk height (2ϵ) in the general case. However, we have also performed a resolution study applying a resolution twice high (or low, respectively), thus using 256×1200 (or 64×300) cells for the whole domain, or 35 (9) cells per disk height. We satisfy the Courant-Friedrichs-Lewy condition by using a CFL number of 0.4.

2.2. Initial conditions

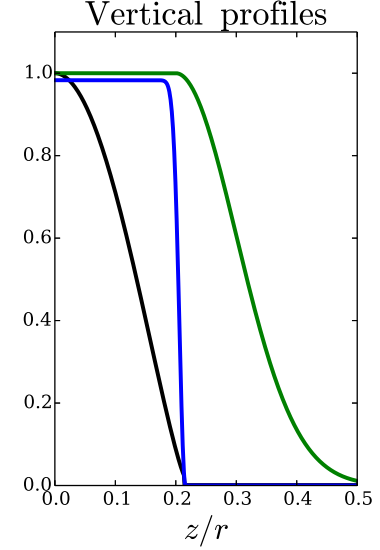


Figure 1. Initial vertical profiles of the disk quantities: density (black, blue shaded), rotational velocity (blue), and magnetic diffusivity F_η (green). The magnetic diffusivity profile is set constant in time.

For the initial conditions we follow a meanwhile standard setup, applied in a number of previous publications (Zanni et al. 2007; Sheikhnezami et al. 2012; Fendt & Sheikhnezami 2013). The initial structure of the accretion disk is calculated as the solution of the steady state force equilibrium,

$$\nabla P + \rho \nabla \Phi_g - \mathbf{J} \times \mathbf{B} - \frac{1}{R} \rho V_\phi^2 (\mathbf{e}_R \sin \theta + \mathbf{e}_\theta \cos \theta) = 0. \quad (7)$$

We solve this equations assuming radial self-similarity, i.e. assuming that all physical quantities X scale as a product of a power law in R with some function $F(\theta)$,

$$X \equiv X_0 R^{\beta_X} F(\theta). \quad (8)$$

Self-similarity requires in particular that the sound speed and the Alfvén speed scale as the Keplerian velocity, $V_K \propto r^{-1/2}$, along the disk midplane. As a consequence, the power law coefficients β_X are determined as follows, $\beta_{V_\phi} = -1/2, \beta_P = -5/2, \beta_\rho = -3/2$, and $\beta_{B_R} = \beta_{B_\theta} = \beta_{B_\phi} = -5/4$.

An essential non-dimensional parameter governing the initial disk structure is the ratio ϵ between the isothermal sound speed $C_s^T = \sqrt{P/\rho}$ and the Keplerian velocity $V_K = \sqrt{GM/r}$, evaluated at the disk midplane, $\epsilon = [C_s^T/V_K]_{\theta=\pi/2}$. This quantity determines the disk thermal scale height $H_T = \epsilon r$. In our simulations we generally assume a thin disk with $\epsilon = 0.1$ initially. Note that for the rest of the paper, when discussing the dynamical properties of disk and outflow, we consider the *adiabatic sound speed* $C_s = \sqrt{\gamma P/\rho}$. The geometrical disk height, namely the region where the density and rotation significantly decrease, is about 2ϵ (see Figure 1). We therefore define the geometrical disk height as $H \equiv 2\epsilon r$.

Following Zanni et al. (2007), our reference simulation is initialized only with a poloidal magnetic field, defined via the vector potential $\mathbf{B} = \nabla \times A \mathbf{e}_\phi$, with

$$A = \frac{4}{3} B_{p,0} r^{-1/4} \frac{m^{5/4}}{(m^2 + ct g^2 \theta)^{5/8}}. \quad (9)$$

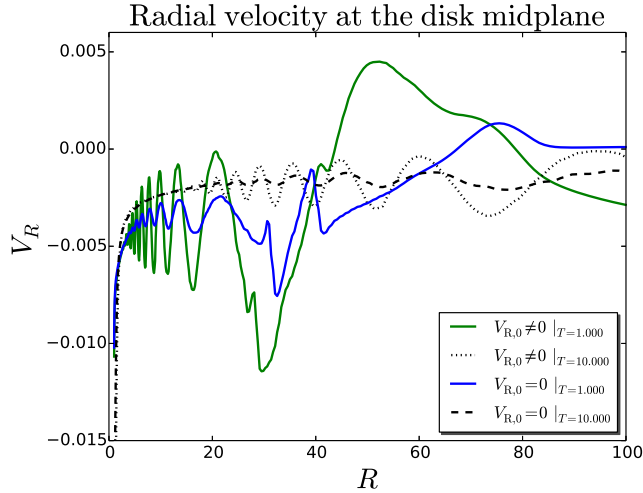


Figure 2. Accretion velocity profile along the disk midplane at $T = 1000$ and $T = 10000$ for the cases of zero and non-zero initial radial velocity.

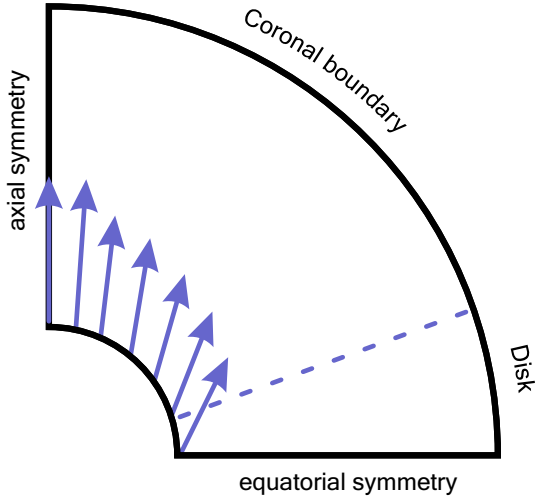


Figure 3. Illustration of the boundary conditions. Along the inner and outer radial boundaries we distinguish two zones - the corona and the disk region. Arrows represent the magnetic field distribution along the inner boundary, which is preserved by our boundary condition.

The parameter $B_{p,0} = \epsilon\sqrt{2\mu_0}$ determines the strength of the initial magnetic field, while the parameter m determines the degree of bending of the magnetic field lines. For $m \rightarrow \infty$, the magnetic field is purely vertical. As we will see below, the long-term evolution of the disk-jet structure is insensitive to this parameter, since due to advection and diffusion processes and the jet outflow, the magnetic field structure is changed substantially over time. We therefore set $m = 0.5$ in general.

The strength of the magnetic field is governed by the magnetization parameter

$$\mu = \frac{B_p^2}{2P} \Big|_{\theta=\frac{\pi}{2}}, \quad (10)$$

the ratio between the poloidal magnetic field pressure and the thermal pressure, evaluated at the midplane, and is set to be constant with radius. As we will see below, the magnetic field distribution substantially changes over time while the disk-jet dynamics is governed by the *actual*

disk magnetization. Typically, the initial magnetization is $\mu_0 \approx 0.01$ in this simulations.

Outside the disk the gas and pressure distribution is defined as hydrostatic "corona",

$$\rho_{\text{cor}} = \rho_{\text{cor},0} R^{-1/(\gamma-1)}, \quad P_{\text{cor}} = \frac{\gamma-1}{\gamma} \rho_{\text{cor},0} R^{-\gamma/(\gamma-1)}, \quad (11)$$

where $\rho_{\text{cor},0} = \delta \rho_{\text{disk}}(R=1, \theta=\pi/2)$ with $\delta = 10^{-3}$,

Although it is common to define the initial accretion velocity, balancing the imposed diffusivity $V_R = \eta J_\phi / B_\theta$, we find that in our set of parameters this is not necessary. It can even disturb the initial evolution of the disk accretion. Accretion requires corresponding torques to be sustained and since there is no initial poloidal current defined, $B_\phi = 0$ (that takes time to build up from a weak poloidal field), a non-zero initial velocity will only lead to extra oscillations. Figure 2 illustrates this issue, showing two identical simulations with zero and non-zero initial accretion velocity. We found that the origin of the oscillations for both cases is the inner boundary. The first wave of accretion is somehow bounced outwards by the inner boundary and results in an oscillatory pattern. We believe that the bouncing at the inner disk boundary is a generic problem of most accretion disk simulations resulting from subtle inconsistencies between the boundary conditions and the intrinsic disk physics. Although they both result in the same final profile (a steady state has been reached only for small disk radii), the simulations with zero velocity profile show fewer oscillations.

2.3. Boundary conditions

We apply standard symmetry conditions along the rotational axis and the equatorial plane. Along the radial boundaries of the domain, we distinguish two different areas. That is (i) a *disk boundary* for $\theta > \frac{\pi}{2} - 2\epsilon^1$, and (ii) a *coronal boundary* for $\theta < \frac{\pi}{2} - 2\epsilon$, and consider different conditions along them (see Figure 3).

Along the inner radial boundary for all simulations we impose a constant slope for the poloidal component of the magnetic field

$$\varphi = 70^\circ \left(1 + \exp\left(-\frac{\theta - 45^\circ}{15^\circ}\right) \right)^{-1} \quad (12)$$

where φ is the angle with respect to unit vector \mathbf{e}_R . The magnetic field direction is axial near the axis, $\theta = 0$, while at the inner disk radius the inclination is 70° with respect to the disk surface. A smooth variation of the magnetic field direction is prescribed along the inner radial boundary. This is in concordance with Pelletier & Pudritz (1992) who showed that for a warm plasma the maximum angle with respect to the disk surface necessary to launch outflows is about 70° , and slightly larger than for a cold plasma (Blandford & Payne 1982).

The method of constraint transport requires the definition of only tangential component, thus to prescribe B_θ along the innermost boundary, while the normal component B_R follows from solving $\nabla \cdot \mathbf{B} = 0$. In order to implement the prescription of a constant magnetic field angle, we solve $\nabla \cdot \mathbf{B} = 0$, taking into account the ratio of the cell-centered magnetic field components

¹ Note, $2\epsilon \approx \arctg(2\epsilon)$

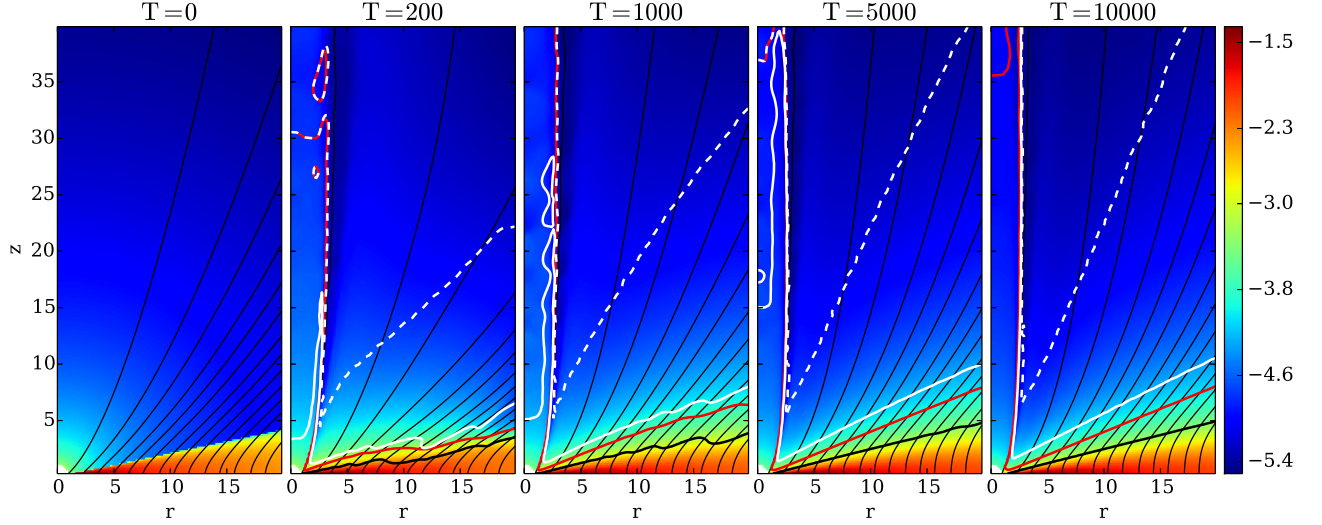


Figure 4. Time evolution of the disk-jet structure for the reference simulation. Shown is the evolution of the density (by colors, in logarithmic scale), the poloidal magnetic field lines (thin black lines), the disk surface (thick black line), the sonic (red line), the Alfvén (white line), and the fast Alfvén (white dashed line) surfaces.

Table 2

Inner and outer boundary conditions. Outflow is zero gradient condition, constant slope conditions are marked by slope in the table.

	ρ	P	V_R	V_θ	V_ϕ	B_R	B_θ	B_ϕ
inner disk	$\sim r^{-3/2}$	$\sim r^{-5/2}$	$\sim r^{-1/2}, \leq 0$	0	$\sim r^{-1/2}$	slope	slope	$\sim r^{-1}$
inner corona	$\sim r^{-3/2}$	$\sim r^{-5/2}$	$0.2\cos(\varphi)$	$0.2\sin(\varphi)$	$\sim r^{-1/2}$	slope	slope	0
outer disk	$\sim r^{-3/2}$	$\sim r^{-5/2}$	outflow, ≤ 0	outflow	outflow	div B = 0	outflow	$\sim r^{-1}$
outer corona	$\sim r^{-3/2}$	$\sim r^{-5/2}$	outflow, ≥ 0	outflow	outflow	div B = 0	outflow	$\sim r^{-1}$

$B_\theta/B_R = -\tan(\varphi)$. We start the integration from the axis ($\theta = 0$), where $B_\theta = 0$. Thus, by fixing the slope of the magnetic lines, we allow the magnetic field strength to vary.

Along the inner coronal boundary, we prescribe a weak inflow into the domain with $V_P = 0.2$. This is just applied to stabilize the inner coronal region between the rotational axis and the disk jet, since the interaction between the current carrying, magnetized jet and zero- B_ϕ coronal region may lead to some extra acceleration of the coronal gas. As it was shown by (Meliani et al. 2006) the pressure of such an inflow (e.g. a stellar wind) may influence the collimation of the jet, changing the shape of the innermost magnetic field lines.

In order to keep the influence of the dynamical pressure of the inflow similar during the whole evaluation (and also for different simulations), we set the density of this inflow with respect to the disk density at the inner disk radius. The density of the inflow corresponds to a hydrostatic corona $\rho_{\text{infl}} = \rho_{\text{cor}} = \rho_{\text{disk}}|_{\text{midplane}}(t) \cdot \delta$, where $\delta = 10^{-3}$. The inflow direction is aligned with the magnetic field direction. By choosing a denser inflow we also increase the time step of our simulations by approximately three times, as the Alfvén speed in the coronal region lowers.

By varying the slope of the magnetic field φ along this inner corona in the range of 60 - 80 degrees, we found that it only slightly affects the slope of the innermost

magnetic field lines. The global structure of the magnetic field is instead mainly governed by the diffusivity model. Since the inner boundary by design models the magnetic barrier of the star, we choose a rather steep slope in order to avoid the disk magnetic flux entering the coronal region.

Across the inner disk boundary (that is the accretion boundary) density and pressure are both extrapolated by power laws, applying $\rho R^{-3/2} = \text{const}$, and $PR^{-5/2} = \text{const}$, respectively. Both the toroidal magnetic field as well as the toroidal velocity components are set to vanish at the inner coronal boundary, $B_\phi = 0$, $V_\phi = 0$. For the inner disk boundary, we further apply the condition $B_\phi \sim 1/r$ ($J_\theta = 0$), and extrapolate the radial and the toroidal velocity by power laws, $V_R R^{-1/2} = \text{const}$, and $V_\phi R^{-1/2} = \text{const}$, respectively, while $V_\theta = 0$.

For the inner disk boundary, only negative radial velocities are allowed, making the boundary to behave as a "sink", thus absorbing all material which is delivered by the accretion disk at the inner disk radius.

As the application of spherical coordinates provides an opportunity to use a much larger simulation domain compared to cylindrical coordinates, the outer boundary conditions have only little influence on the evolution of the jet launched from the very inner disk. We therefore extrapolate ρ and P with the initial power laws and apply the standard PLUTO outflow conditions for V_R, V_θ, V_ϕ at the outer boundary, thus zero gradient conditions. We

further require $B_\phi \sim 1/r$ ($J_\theta = 0$) for the toroidal magnetic field component, while a simple outflow condition is set for B_θ . Again B_R is obtained from the $\nabla \cdot \mathbf{B} = 0$.

For the radial velocity component we distinguish between the coronal region, where we require positive velocities $V_R \geq 0$, and the disk region, where we enforce negative velocities $V_R \leq 0$.

As our application of a spherical geometry is new in this context, we summarize the boundary conditions in the Table 2.

2.4. The magnetic diffusivity model

Accretion disks are considered to be highly turbulent, subject to the magneto-rotational instability (MRI) in moderately magnetized disks (Balbus & Hawley 1991; Fromang 2013), and the Parker instability (Gressel 2010; Johansen & Levin 2008) for stronger magnetized disks. It is believed that when the magnetic field becomes sufficiently strong the MRI modes become suppressed (Fromang 2013). On the other hand, a strong magnetic field may become buoyant, leading to the Parker instability. While the MRI is confined within the disk, the Parker instability operates closer to the surface of the disk where the toroidal magnetic field is stronger.

In order to extrapolate the results from a self-consistent, local treatment of turbulence to the mean field approach is not straightforward. In the local treatment the extraction of angular momentum is due to both turbulence - operating on small scales - and torques by the mean magnetic field on large scales. Thus, removal of angular momentum goes hand in hand with destroying of the turbulent magnetic field or the effective magnetic diffusivity. In case of the mean field approach, there is no small scale turbulence and, thus, no angular momentum removal by local turbulent motions. Here, the diffusivity plays only a role for leveling out the magnetic field gradient, thus setting the overall structure of the magnetic field. Unfortunately, we lack the complete knowledge of the disk turbulence, thus the connection between the mean magnetic field and the fluctuating part. Or, in other words, the relation between the mean magnetic field and the effective torques, and the diffusivity and viscosity that turbulence provides. We believe that when moving from a local turbulence approach to the mean field approach, the relevance of the model should be approved by the relevance of the magnetic field distribution itself, and not by the diffusivity model. However, one should keep in mind that the magnetic field strength and structure of real accretion disks are also not known. Therefore, when considering any simulation results, always the diffusivity model applied should be taken into account.

A self-consistent study of the origin of the turbulence is beyond the scope of our paper. We therefore prescribe a certain model of the magnetic diffusivity. We apply an α -prescription (Shakura & Sunyaev (1973)) for the magnetic diffusivity, implicitly assuming that the diffusivity has a turbulent origin. The diffusivity profile may extend up to one disk height above the disk surface (Figure 1).

Although we investigate different diffusivity models, all of them can be represented in a following form,

$$\eta_P = \alpha_{\text{ssm}}(\mu) C_s \cdot H \cdot F_\eta(z), \quad (13)$$

where the vertical profile of the diffusivity is described

by a function

$$F_\eta(z) = \begin{cases} 1 & z \leq H \\ \exp(-2(\frac{z-H}{H})^2) & z > H, \end{cases}$$

confining the diffusivity to the disk region.

Although this parametrization of diffusivity is commonly used (except the profile function $F_\eta(z)$), there are no clear constraints upon the value α_{ssm} may take. As an example, King et al. (2007) discuss a magnitude of the turbulent α -parameter derived from observations and simulations, indicating observational values $\alpha_{\text{ssm}} \simeq 0.1..0.4$. Numerical models with zero net magnetic field usually provide low numerical values $\alpha_{\text{ssm}} \simeq 0.01$, reaching at most $\alpha_{\text{ssm}} \simeq 0.03$ (Stone et al. 1996; Beckwith et al. 2011; Simon et al. 2012; Parkin & Bicknell 2013). On the other hand, numerical modelling of the MRI applying a non-zero net magnetic field (Bai & Stone 2013) indicate substantially higher values, $\alpha_{\text{ssm}} \simeq 0.08 - 1.0$, with a corresponding magnetization $\mu = 10^{-4}, 10^{-2}$.

Obviously, different functions of $\alpha_{\text{ssm}}(\mu)$ will lead to different evolution. We start from the well-known model for magnetic diffusivity applied by many authors before (Casse & Keppens 2004; Zanni et al. 2007; Sheikhezhani et al. 2012),

$$\eta_P = \alpha_m V_A \cdot H \cdot F_\eta(z) \quad (14)$$

by applying $\alpha_{\text{ssm}} = \alpha_m \sqrt{2\mu}$, where $V_A = B_P / \sqrt{\rho}$ is the Alfvén speed, and μ , C_s , and H are the magnetization, the adiabatic sound speed and the local disk height, respectively, measured at the disk midplane. We evolve α_{ssm} and C_s in time, but for the sake of simplicity we keep H and $F_\eta(z)$ constant in time, thus equal to the initial distribution. The main reason is to avoid additional feedback, which favors the accretion instability (see below, or e.g. Campbell (2009)). Our test simulations evolving the disk height in time, in fact indicate the rise of such instability earlier than in case of a fixed-in-time disk diffusivity aspect ratio.

2.5. Anisotropic diffusivity

In general, the diffusivity tensor has diagonal non-zero components,

$$\eta_{\phi\phi} \equiv \eta_P \quad \eta_{RR} = \eta_{\theta\theta} \equiv \eta_T, \quad (15)$$

where we denote η_P as the *poloidal* magnetic diffusivity, and η_T as the *toroidal* magnetic diffusivity, respectively. The anisotropy parameter $\chi \equiv \eta_T / \eta_P$ quantifies the different strength of diffusivity in poloidal and toroidal directions.

In the literature it is common to assume χ of order the of unity. Considering viscous disks, Casse & Ferreira (2000) showed that there is a theoretical limit for η_T , namely $\eta_T > \eta_P$. Highly resolved disk simulations indeed suggest $\chi \simeq 2..4$ (Lesur & Longaretti 2009), implying that the toroidal field component is typically diffusing faster than the poloidal component.

The majority of simulations in the literature consider a magnetic field strength in equipartition with the gas pressure. However, studying also weakly magnetized disks, we find that there also exists an upper limit for the anisotropy parameter, above which the simulations show an irregular behaviour. On the other hand, it was pointed out by several authors (see e.g. Zanni et al.

2007) that in case of a very low anisotropy parameter (thus, a weak toroidal diffusivity) the simulations might suffer from instabilities caused by strong pinching forces. Nonetheless, the existence of an upper limit for the anisotropy parameter was so far obscured by other processes.

Assuming a steady state and combining the poloidal component of the diffusion equation, $M_R = \alpha_{\text{ssm}} H J_\phi / B_P$, with the relation for the Mach number $M_R = 2 / \sqrt{\gamma} H J_R / B_P \mu_{\text{act}}$ (see below, Königl & Salmeron 2011), an interrelation between the toroidal and poloidal electric currents can be derived,

$$\frac{J_\phi}{J_R} = \frac{\sqrt{2\mu}}{\sqrt{\gamma}\alpha_m}. \quad (16)$$

This relation has been proven to approximately hold for all of our simulations, thus indicating that a steady state has indeed been reached. Since the only free parameter in this relation is α_m , the choice of α_m governs the ratio of the electric current components.

As shown previously (Ferreira & Pelletier 1995; Ferreira 1997; Ferreira & Casse 2013) the toroidal component of the induction equation can be written as

$$\eta_T J_R|_{\text{mid}} = -R^2 \int_0^{2\epsilon} \mathbf{B}_P \cdot \nabla \Omega d\varphi - V_\theta B_\phi \quad (17)$$

(here expressed for spherical coordinates), where J_R is computed at the disk midplane. This equation essentially states that the induction of the toroidal magnetic field component (from twisting the poloidal component) is being balanced by the diffusion through the disk midplane and by escape of the flux through the disk surface. We emphasize that we do *not* neglect the $V_\theta B_\phi$ term, considering the assumption of a thin disk (Ferreira & Casse 2013), as we find it of key importance in our simulations, in particular in the regime of a moderately strong magnetic field, $\mu \geq 0.1$.

Assuming that the induction of the magnetic field is primarily due to radial gradients, the radial component of the magnetic field can be approximated by a power law, $B_R \propto R^{-5/4}$, and equation 17 may be transformed into $\eta_T J_R|_{\text{mid}} \simeq B_R C_s - V_\theta B_\phi$, or

$$(\alpha_{\text{ssm}} \chi - M_\theta) J_R \simeq \frac{B_R}{H}, \quad (18)$$

where

$$M_\theta = -V_\theta^+ / C_s \quad (19)$$

is denoted as the ejection Mach number, where V_θ^+ is measured at the disk surface.

Using relation 16 between the poloidal and toroidal electric currents and defining the curvature part of the toroidal current $J_\phi^{\text{curv}} \equiv B_R / H$, one may derive a constraint for the anisotropy parameter,

$$\frac{J_\phi^{\text{curv}}}{J_\phi} \simeq \left(\alpha_m \chi - \frac{M_\theta}{\sqrt{2\mu}} \right) \alpha_m \leq 1. \quad (20)$$

Any magnetic field geometry which is outwardly bent and has a decreasing field strength in outward direction has to satisfy this relation, as J_ϕ consists of two positive terms, the gradient and the curvature. In cases where the vertical velocity term can be neglected (e.g. for a very

weak magnetic field with $\mu \leq 0.02$), the anisotropy parameter is $\chi < 1/\alpha_m^2$, which for our choice of α_m is about 0.4. By probing the χ parameter space we found that in order to obtain a stable accretion-outflow configuration for weakly magnetized disks, the χ should be in the range 0.3–0.7. We therefore decided to apply $\chi = 0.5$ for all of our simulations. We note that in simulations applying an anisotropy parameter $\chi \geq 0.7$, we faced the problem that the poloidal magnetic field lines were "moving" rapidly, such that the bending of the field lines along the disk midplane was actually inverted. This is a result of the combined effects of a strong outward diffusion and low torques at the midplane. On the other hand, in case of a rather low anisotropy parameter, the accretion is rapid and the jet does establish a steady behaviour.

The reason why the commonly chosen anisotropy $\chi > 1$ leads to a steady behaviour is rather simple. As the disk magnetization grows during advection, the ejection Mach number grows as well (we find that $M_\theta \propto 6\mu$ saturating at a level of 0.8, see below). Thus in case of a high disk magnetization - usually assumed in the literature - the above mentioned upper limit for the anisotropy parameter is satisfied. In case of weak magnetic field simulations, performed e.g. by Murphy et al. (2010), this limit is most likely satisfied by additional viscous torques.

2.6. Comparison to previous simulations

In the introduction section we have already discussed the literature of accretion-ejection simulations. Here we want to explicitly emphasize specific details in which our simulations differ from previous works.

- A spherical grid has been applied, offering the opportunity of a much larger domain size as well as much higher resolution *in the inner part* of the disk. A new set of boundary conditions is used that is adapted to the spherical grid.
- We were able to explore a continuous range of simulation parameters. In particular we were aiming to disentangle interrelations between the *actual* flow parameters, rather than an interrelation to the initial values.
- Altogether, our model setup allows very long term simulations on a large grid - so far we have run simulations for approximately 30,000 time units for a standard diffusivity model, and more than 150,000 time units for our modified strong diffusivity model.
- We allow the inflow (into the coronal region) density to vary in time, thus keeping the ratio between the inflow and the disk densities δ the same as initially.

We have explored a vast range of the parameter space that covers the majority of simulations performed in the literature (see Table 3). Similar to all these papers we assume a thin disk $\epsilon = 0.1$. It is common to assume a magnetic diffusivity parameter α_m of about unity. In our case we apply values $\alpha_m = 1.1 \dots 1.9$. For the magnetic field bending parameter we have chosen $m = 0.5$, which is slightly higher than the values usually adapted, $m = 0.35 \dots 0.4$. Although we finally show that m plays

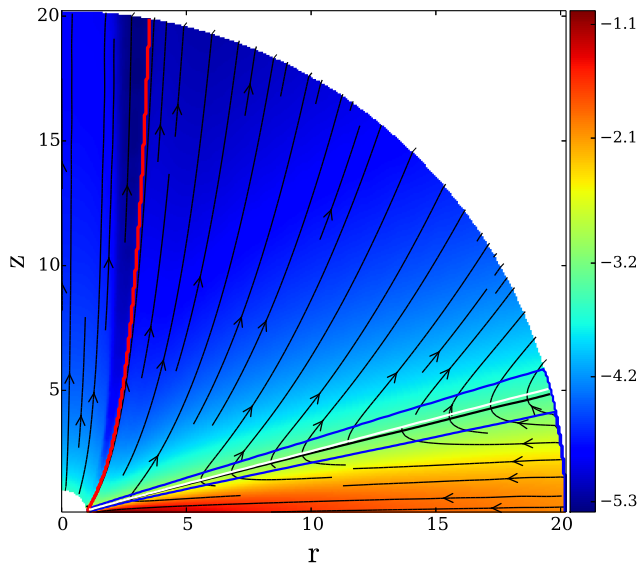


Figure 5. Physically different regions of the disk-jet structure at $t = 10,000$. Shown is the mass density (in logarithmic scale) and streamlines of the poloidal velocity (black lines with arrows). Red line marks the magnetic field line rooted at in innermost area of the midplane. Upper blue line separates from the disk an area where $V_p || B_p$. The accretion and ejection areas are separated with white ($V_r = 0$) and black ($F_\phi = 0$) lines, respectively. The lower blue line separates the accretion area where $V_r \gg V_\theta$ from the rest of the structure.

only a minor role, our choice is motivated by the fact that this value is more consistent with the inner boundary condition. The magnetic diffusivity anisotropy parameter χ is chosen smaller than unity, since it helps keeping sufficiently strong torques at the midplane and the bending of the magnetic field that supports launching.

Although we start our simulation from a moderately weak initial magnetic field, the actual field strength in the inner disk at a certain radius may vary substantially over time. This allows us to study the interrelation between disk accretion and ejection physics and the *actual* magnetic field strength (thus the actual disk magnetization).

3. A REFERENCE SIMULATION

In this section we present our reference simulation. Our aims were two-fold. First, with our new setup we were able to increase both the period of time evolution and the spatial extension of jet launching conditions considerably compared to previous works. Second, with our long-term evolution simulations we were able to investigate the interrelation between the *actual* disk properties such magnetization, the ejection to accretion ratios of mass and energy, jet velocity, and others. This has not been done in the past, as most papers have compared the *initial* parameters of the simulations. As shown by Sheikheezami et al. (2012) both the magnetization and diffusivity may substantially change during the disk evolution, and the parameters for the initial setup μ_0 or α_{ssm} are not sufficient to characterize the disk-jet system.

In order to uniquely specify the *initial conditions* for the simulation, we prescribe a number of non-dimensional characteristic parameters. The *initial* disk height is set by ϵ . For all simulations we apply $\epsilon = 0.1$. The *initial* strength and structure of the magnetic field is set by μ_0 and m , respectively. In all simulations we

have chosen $m = 0.5$.

The initial disk magnetization does not play a major role in the *jet launching* process, but it is responsible for the overall disk torques. The main reason is that the magnetization in the inner disk, from which the main jet is being launched, changes very quickly. However, the magnetic field in the overall disk is primarily set by the initial magnetization.

In our simulations we examine $\mu_0 = (0.003, 0.01, 0.03)$.

The model for diffusivity is chosen by selecting the distribution $\alpha_{ssm}(\mu)$ and the anisotropy parameter χ . We also set $\chi = 0.5$ for all simulations. We apply a standard diffusivity model (Equation 14), thus the diffusivity is set by the α_m parameter. As will be shown later, the simulations are very sensitive to this parameter. If not stated otherwise, $\alpha_m = 1.65$.

We will refer to our reference simulation as to the setup with $\epsilon = 0.1, m = 0.5, \mu_0 = 0.01, \alpha_m = 1.65, \chi = 0.5$. Usually we run the simulations until $t = 10,000$, corresponding to about 1600 orbits at the inner disk radius.

Figure 4 shows the time evolution of the disk-jet structure of the reference simulation. Note that here we present only a small cylindrical part of a much larger, *spherical* domain. Although we explore a broad parameter space, the evolution for this simulation can be seen as a typical.

The first snapshot shows the initial state - a hydrodynamic disk in force-balance, the non-rotating hydrostatic corona in pressure equilibrium with the disk, and the initial non-force-free magnetic field. After some 1000 revolutions, the inner parts of the disk-outflow reaches a quasi steady state. However, it takes much longer time for the outer parts to reach such a state. The outflow, initiated already at early times and constantly accelerated, finally reaches super-fast magnetosonic speed. The outflow launching area along the disk surface grows with time. However, the parts of the outflow being launched from larger disk radii are less powerful.

This reference simulation applying typical parameters from the literature can be re-established very well by our approach. Using a spherical setup, the resolution in the inner part of the disk is higher than in the literature, and the simulations run substantially longer than any other simulation published before. Our simulations behave very robust. We believe that there are two main reasons for that. First, the spherical geometry does well resolve the inner part of the disk, from which the dominant part of the jet is launched, but smooths out the small scale perturbations in the outer disk. By that, perturbations arising throughout the disk are diminished. Second, our choice for the diffusivity parameter α_m allows to evolve the simulations into a quasi steady state in which advection is balanced by diffusion. However, even with such an optimized numerical setup (the reference setup) our simulations show some irregular behaviour typically at about 30,000 time units. The reason is that since the current diffusivity model is prone to the accretion instability (see Lubow et al. 1994, and section below), the simulations are always in a state of marginal stability. As a consequence, the simulations evolve into a state of either high or low magnetization. In case of high magnetization the structure of the inner disk is being drastically changed and current model of diffusivity cannot be applied. In the opposite case of weak magne-

Table 3

Comparison of our simulations with simulations performed by other authors. The resolution is estimated for the *inner* disk ($R = 1$)

Reference	cell/ 2ϵ	ϵ	m	α_m	χ	μ_0	μ_{act}
Casse & Keppens (2004)	0.5	0.1		< 1	1	$\simeq 1$	-
Zanni et al. (2007)	2.5	0.1	0.35	0.1 ... 1.0	1, 3	0.3	-
Tzeferacos et al. (2009)	2.5	0.1	0.4	0.1 ... 1.0	3, 100	0.1-3.0	-
Sheikhnezhani et al. (2012)	8.0	0.1	0.4	1.0	1/3, 3	0.002-0.1	-
This work, reference simulation	16	0.1	0.2-0.9	1.1-1.9	0.5	0.003-0.03	0.001-0.5
This work, resolution study	24.5	0.1	0.2-0.9	1.1-1.9	0.5	0.003-0.03	0.001-0.5

tization stable jets cannot be sustained.

In the following, we discuss different components of the disk-jet system and the jet launching and acceleration mechanism. We define how we measure certain disk properties, such as the location of the disk surface or the mass fluxes in the physically different areas. We explore the role of the diffusivity, the strength and geometry of the magnetic field in respect to the outflow and accretion rates.

3.1. Disk structure and disk surface

We define the disk surface as a surface where the *radial velocity changes sign*. In a steady state the area where the radial velocity and the magnetic torque changes sign is almost identical.

Figure 5 shows the typical structure of the disk-jet system. Several, physically different regions can be distinguished - the inflow area, the jet acceleration area, the launching area, and the accretion domain. These are separated by colored lines. White and black lines mark the disk surface that separates disk and corona regions. Two other lines separate the accretion, launching and acceleration areas. We define the *accretion region* as the area where velocity is mainly radial, $V_\theta < 0.1V_R$, and the *acceleration region* as the area where the flow velocity is parallel to the magnetic field, $\sin(\text{angle}(\mathbf{B}, \mathbf{V})) < 0.1$. As the *launching area* we characterize the region in between.

In our simulations, the position of the disk surface as defined above remains about constant in time. This confirms our choice of the control volume (see below) and our choice to fix the diffusive scale height during the simulation.

According to our boundary conditions we prescribe a weak inflow into the region between the inner disk radius and the rotational axis. This inflow provides the matter content as well as the pressure balance along the rotational axis. The astrophysical motivation can be the presence of a central stellar magnetic field or a stellar wind. In Figure 5 the inflow area is the area between the rotational axis and the red line that marks the magnetic field line rooted in the inner disk radius at the midplane. In all figures below the magnetic field line closest to the axis always corresponds to the magnetic field line anchored at the inner disk radius².

² Note that there are magnetic field lines which still penetrate the disk, but are not rooted at the disk midplane. These lines originate from inside the inner disk radius and are considered as intermediate between the axial coronal region and the main disk outflow. The pure inflow, which is prescribed from the coronal region along the inner boundary, is moving with the injection speed, thus is not accelerated.

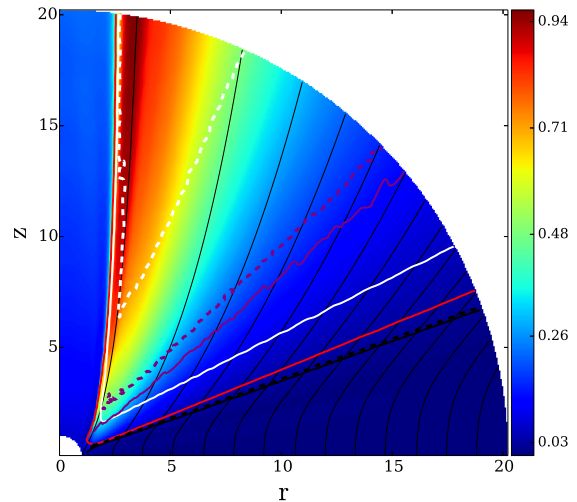


Figure 6. Importance of the Lorentz force with respect to the pressure and centrifugal forces for reference simulation at $T = 10,000$. Shown is the poloidal speed (by colors), the poloidal magnetic field (black thin lines). Alfvén (white), fast-magnetosonic (dashed white), sonic (red) surfaces. Thick black lines denote the surface where Lorentz force is equal to pressure force components: parallel (dashed) and perpendicular (solid) to the magnetic field. Thick purple lines denote the surface where Lorentz force is equal to centrifugal force components: parallel (dashed) and perpendicular (solid) to the magnetic field. Thin black lines denote the ratios of Lorentz force components: parallel (left) and perpendicular (right) to magnetic field.

3.2. Launching mechanism

Here we briefly comment on the jet launching mechanism in our reference simulation that is - as in previous simulations - the Blandford-Payne magneto-centrifugal driving.

As demonstrated above (see Figure 5), the magnetic torque rF_ϕ changes sign on the disk surface. It is negative in the disk and positive in the corona. Thus, the magnetic field configuration established extracts angular momentum from the disk. The angular momentum extraction relies on the induced toroidal magnetic field component which plays a key role in transferring the angular momentum $\sim B_r B_\phi$. Gaining angular momentum, the material that is loaded to the field lines from the accretion disk is pushed outwards by the centrifugal force.

In order to illustrate the acceleration process, we show the magnitude of Lorentz force with respect to the thermal pressure and centrifugal forces. Figure 6 shows the contours where the perpendicular and parallel components of the Lorentz force are equal to the perpendicular and parallel components of pressure and centrifugal force, respectively. In the accretion disk both the

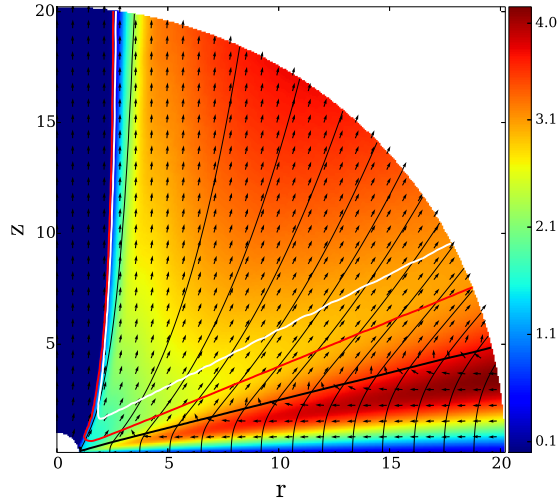


Figure 7. The ratio of the toroidal to poloidal magnetic field for the reference simulation at $T = 10,000$. Lines represent the disk (thick black line) the sonic (red line), the Alfvén (white line) surfaces. Arrows show normalized velocity vectors.

pressure and the centrifugal forces dominate the poloidal component of the Lorentz force. Below the disk surface the Lorentz force (toroidal component) extracts the angular momentum from the disk.

Since the Lorentz force increases along the outflow, it is worth to check the decomposed Lorentz force components $F = \nabla \times B \times B$ in the directions parallel and perpendicular to the magnetic field (Ferreira 1997). The ratio between toroidal and parallel components of the magnetic field,

$$\frac{F_{||}}{F_{\phi}} = -\frac{B_{\phi}}{B_p}, \quad (21)$$

is shown in Figure 7. We see that the centrifugal force is stronger in the inner area of the disk rather than in the outer parts of the disk.

At the sonic surface, the Lorentz force overcomes the pressure forces. From this point on the main acceleration force is the centrifugal force. Further along the outflow - between the Alfvén surface and the fast surface - the Lorentz force becomes the main accelerating force.

3.3. Mass flux evolution

We now explore the mass flux evolution namely the accretion and ejection rates.

In θ -direction the control volume is enclosed by the disk surface (as defined above) S_S and the disk midplane. The two other surfaces which enclose the control volume are marked by S_1 and S_R , and correspond to the vertical arcs at the innermost disk radius ($R = 1$) and at any other radius R . The control volume defined by these surfaces is denoted by $V(R)$.

Thus, the disk mass enclosed by a radius R follows from

$$M(R) = 2 \int_{V(R)} \rho dV, \quad (22)$$

while the mass accretion rate at a certain radius R is

$$\dot{M}_{\text{acc}}(R) = -2 \int_{S_1}^{S_R} \rho \mathbf{V}_p \cdot d\mathbf{S}, \quad (23)$$

and the mass ejection rate is integrated along the disk surface,

$$\dot{M}_{\text{ej}}(R) = -2 \int_{S_S} \rho \mathbf{V}_p \cdot d\mathbf{S}. \quad (24)$$

The mass accretion rate is defined positive if it increases the mass in the control volume. The mass ejection rate is defined positive if it decreases the mass of the control volume. The factor of two in front of the integrals takes into account the fact that only one hemisphere is treated. Note also a minus sign in front of the integrals.

It is common to introduce the ejection index ξ which is based on the mass conservation law for a steady solution (Ferreira & Pelletier 1995). It basically measures the steepness of the radial profile of the accretion rate along the midplane. Setting the outer radius to r and the inner radius to unity, the ejection index interrelates ejection and accretion,

$$\frac{\dot{M}_{\text{ej}}}{\dot{M}_{\text{acc}}} = 1 - r^{-\xi}. \quad (25)$$

We obtain the ejection index by a linear approximation of $\xi = -\log(1 - \dot{M}_{\text{ej}}/\dot{M}_{\text{acc}})/\log(r)$ within $r = [2, 10]$. The higher the ejection index, the higher the fraction of accreted matter being ejected within a given radius, and the less matter reaches the inner boundary. For our reference simulation $\xi \simeq 0.3$ at $T \simeq 10,000$.

Although the disk continuously loses mass (Figure 8), after dynamical times 1000-2000 the disk mass loss is much smaller than the corresponding ejection and accretion rates. We therefore state that the simulation evolves through a series of quasi steady states. We find that a continuous disk mass loss is a typical feature of a simulation like our reference simulation. This is because the mass accretion from outside some outer disk radius is not able to sustain the mass which is lost by accretion and ejection within this radius. We also find that the standard diffusivity model typically leads to a *magnetic field* distribution in the disk that is almost constant in time (not in space). These two facts result in an increase of the disk magnetization in the inner disk, that in turn leads to a more rapid accretion in the inner disk.

Figure 8 shows the time evolution of the mass accretion and ejection rates. Note also the general decrease of the mass fluxes over time, which is a direct consequence of the decrease of the disk mass. The behaviour and actual values of the mass fluxes are typical to the literature values. One should notice two distinct features of the mass fluxes. First, the higher integration volume, the higher the mass ejection rate. Second, in jet launching disks the mass accretion rate must increase with the radius. These plots also indicate that the evolution of the system can be seen as a consecutive evolution through a series of quasi steady states.

3.4. Magnetic field bending parameter study

Here we discuss simulations, investigating the influence of the initial magnetic field bending parameter m . We have varied m from 0.2 (strongly inclined) to 0.9 (almost vertical).

Our main result is that, although the simulations evolve slightly different initially, on the long-term evolution they are almost indistinguishable.

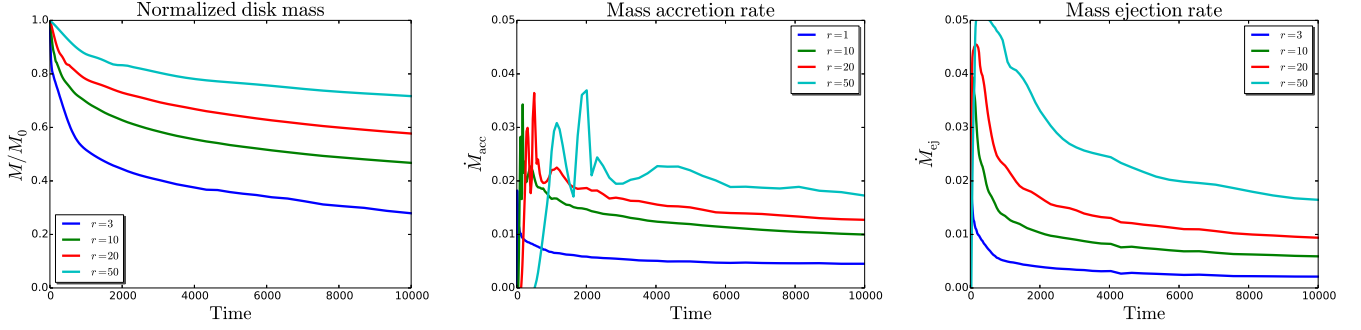


Figure 8. Time evolution of the disk mass (left), the mass accretion rate (center) and the mass ejection rate (right) of the reference simulation at different radii.

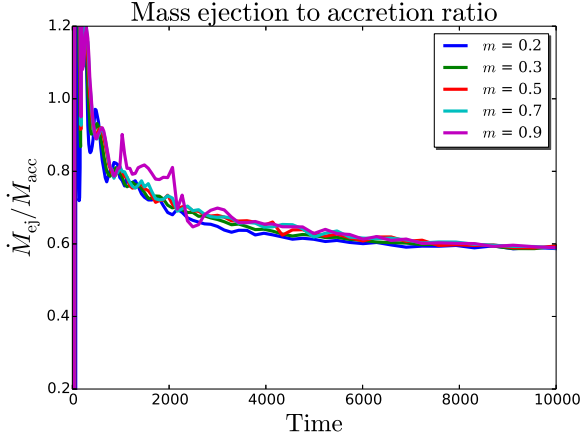


Figure 9. Time evolution of the mass ejection to accretion ratio for simulations evolving from an initial magnetic field distribution with different initial bending parameter m .

Figure 9 shows the time evolution of the ejection to accretion mass flux ratio. The fluxes are again computed for the control volume extending to $R = 10$. It seems to take a few 1000 dynamical time steps for the simulation to lose the memory of the initial magnetic field configuration, but at $t = 10,000$ convergence has been obviously reached. This is also true for the fluxes of angular momentum and energy, and holds as well for the corresponding flux ratios.

The reason why the simulations converge into a single - specific - configuration is the fact that it is mainly the diffusivity model that governs the evolution of the magnetic field evolution. When we start the simulations with the same initial magnetic field strength at the mid-plane, this results in exactly the same magnetic diffusivity profile. Since we explore rather weak magnetic fields (weaker than the equipartition field), the underlying disk structure cannot be changed substantially by the Lorentz force. In contrary, the magnetic field distribution adjusts itself in accordance with the diffusivity model, which has the same vertical profile ab initio.

The convergence we observe for these simulations, starting from an initial magnetic field with different bending, again confirms the reliability of our model in general.

3.5. Resolution study

Here, we briefly present example results of the resolution study. We have performed simulations with a grid resolution of (0.5, 0.75, 1.0, 1.5, 2.0)-times our standard

resolution of 128 cells per quadrant, corresponding to (64, 96, 128, 192, 256) cells per quadrant, or approximately (8, 12, 16, 24, 32) cells per disk height 2ϵ . Note that once the resolution in θ -direction and the radial extent of the disk is chosen, the resolution in R -direction is uniquely determined (see Section 2.1).

For the resolution study all simulations were performed up to typically 10,000 time units. Figure 10 shows snapshots of some of these simulations. Essentially, we see an almost identical disk-outflow structure, indicating that numerical convergence has indeed been reached.

Figure 11 shows the time evolution of the mass ejection to accretion ratio, again integrated throughout the control volume $R < 10$, for simulations of a different resolution. We notice two particular issues. First, all curves bunch together at the mass ejection-to-accretion ratio of about 0.6, indicating convergence of the simulations (this is also true for other flux ratios). Second, the simulation with the highest resolution show some intermittent behaviour (see Figure 10). This might be related to the spatial reconstruction in non-Cartesian coordinates close to the symmetry axis or to the ability to resolve more detailed structures. We conclude that for the resolution chosen our simulations have converged for the launching region.

Note that although the spherical grid is beneficial for disk and outflow launching studies, mainly due to the higher resolution of the inner disk, its application to the jet propagation further away from the jet source is limited because of the lack of resolution at larger radii.

4. MAGNETIZATION ANALYSIS

In the following we investigate a number of physical processes of jet launching by comparing different simulations similar to the reference simulation.

As we have mentioned above, the evolution of our reference simulation can be seen as a sequence of quasi-steady states. The slow, but constant decrease of the disk mass eventually leads to the change of the disk magnetization. This is more prominent in the inner part of the disk, whereas the magnetization of the outer disk does not change too much. This feature brings the opportunity of studying the disk and jet quantities with respect to the *actual* disk magnetization.

In this section we present a set of simulations similar to our reference simulation, however applying a slightly different choice of parameters. The reference simulation was chosen such that diffusive processes are in balance with advective processes. Now, by choosing a slightly different diffusivity parameter α_m , these processes now

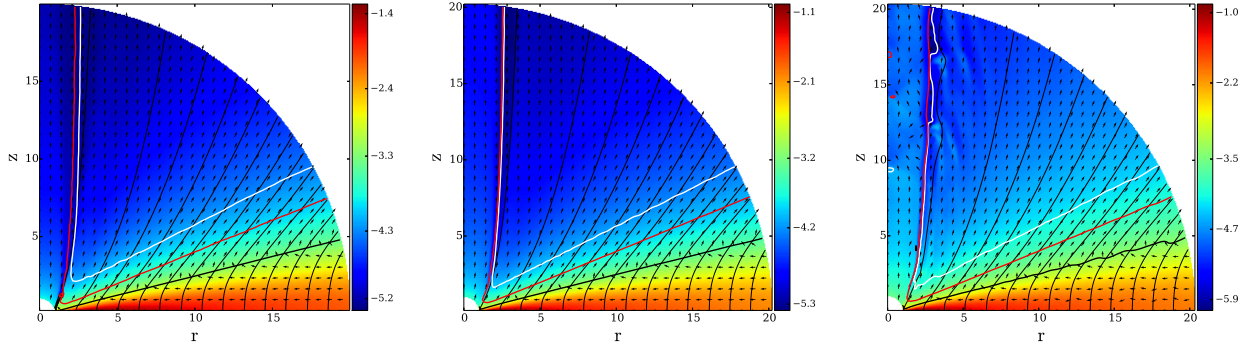


Figure 10. Resolution study. Shown are snapshots of the density distribution at $t = 10,000$ for simulations with different resolution. From left to right the resolution is (8, 16, 32) cells per disk height ($2e$). Black lines mark the magnetic field lines (plotted as flux surfaces). Lines represent the disk (thick black line) the sonic (red line), the Alfvén (white line) surfaces. Arrows show normalized velocity vectors.

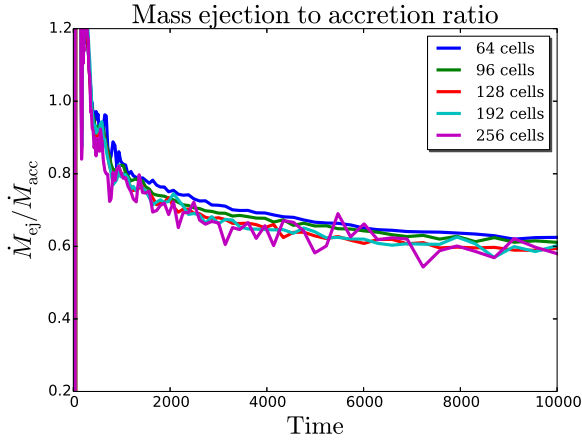


Figure 11. The evolution of the ejection-to-accretion ratio at $R=10$ for the reference simulation with different resolution.

are out of the balance. This leads either to further faster advection or diffusion of the magnetic field. Naturally, in case of lower α_m , advection dominates, and, thus, magnetization grows, leading to even faster advection. In the opposite case, the disk magnetization decreases.

This approach allows us to study the evolution of the accretion-ejection in a very general way. Each of the simulations applied has started from the same initial conditions, however, it now follows a different evolutionary track and finally evolves into a quite different state of the system.

Figure 12 shows the time evolution of the disk mass, the average magnetization of the inner disk (averaged between $R = 1.1$ and $R = 1.5$), and the jet speed here defined as

$$V_{\text{jet,act}} \equiv \max(V_P)|_{R=100}, \quad (26)$$

the maximum jet speed obtained at $R = 100$, considering only those magnetic field lines rooted in the disk.

We emphasize that the jet speed as computed here is only an extrapolation of the terminal jet speed (at infinity). The general behaviour of the disk is as follows. First, the different simulations behave rather similar. After some time they start to differ from each other. At later stages the disks and their outflows arrive at definitely different dynamical states. The exact times at which this happens, depends of course on the radius for which we examine of the disk properties. Figure 12 shows this evolution in the disk and jet quantities for the inner

disk. Therefore the time when simulations start showing differences is rather small, about few hundred dynamical time steps.

Since we start the simulation with *no* accretion, initially diffusion is not in balance. However, electric currents are induced quickly within the disk, and subsequent angular momentum transport results in accretion. Depending on the value of diffusivity parameter α_m the system results either in advection-dominated regime (for $\alpha_m < 1.65$), or diffusion dominated regime ($\alpha_m > 1.65$). In principle an equilibrium situation is possible in which these two processes are in balance. In case of $\mu_0 = 0.01$, the diffusivity parameter for an equilibrium situation is around $\alpha_m = 1.65$. We will refer to the *critical* diffusivity parameter α_{cr} as the one corresponding to the equilibrium state when advection and diffusion balance each other. Generally, the lower the diffusivity, the stronger the advection and thus the resulting magnetization.

We confirm Tzeferacos et al. (2009) finding that in case of a strong magnetic field with $\mu \sim 0.3$ the disk structure changes substantially - the disk becomes much thinner in the inner region of the disk. A stronger magnetic field exerts a stronger torque on the disk, leading to a faster accretion rate. Thus, at some point in time the accretion velocity becomes supersonic, $M_{R,act} > 1$. We consider this as the limit for applying our magnetic diffusivity model.

As clearly visible from the figures discussed above, for the present setup the current diffusivity model (Equation 14) is only marginally stable - all deviations from the critical diffusivity will be further amplified. If magnetic diffusion dominates the disk, the magnetic field becomes weaker and weaker unless at about $\mu \sim 0.001$ the jet outflow cannot be sustained anymore. On the other hand, a weaker diffusivity leads to a faster accretion that also results in a runaway process. One way to circumvent this problem is to apply a different model for the diffusivity, namely $\alpha_{ssm}(\mu)$ (see Section 5).

As might be easily seen from Figure 12, ongoing disk mass depletion in most cases leads to a higher degree of disk magnetization, a process which happens faster for less diffusive, thus higher advective simulations. A change in magnetization may substantially changes the dynamics of the disk. The stronger magnetization, for example, leads to higher jet speed.

One might notice the deviation in the behaviour of the jet terminal speed for the low value of α_m . We believe that this results from the position where we calculate

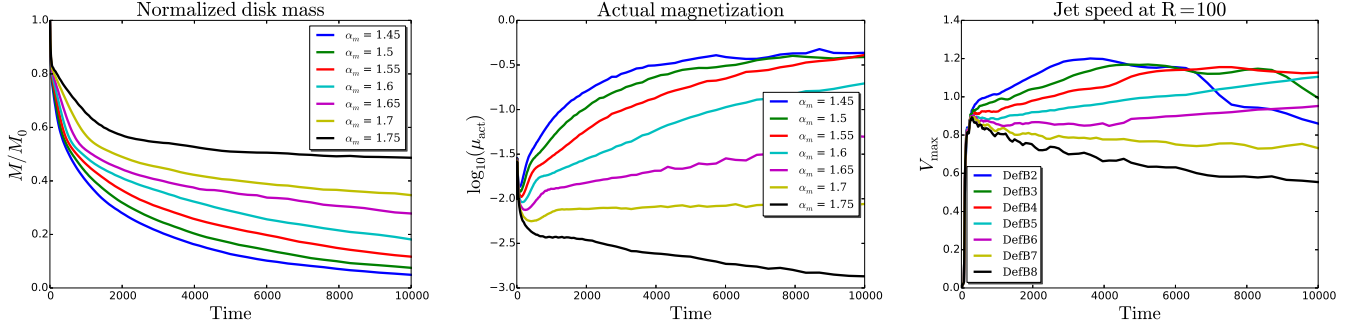


Figure 12. Time evolution of the normalized disk mass (left), the actual magnetization of the disk (center), and the jet terminal speed (right) for different diffusivity (α_m) strength.

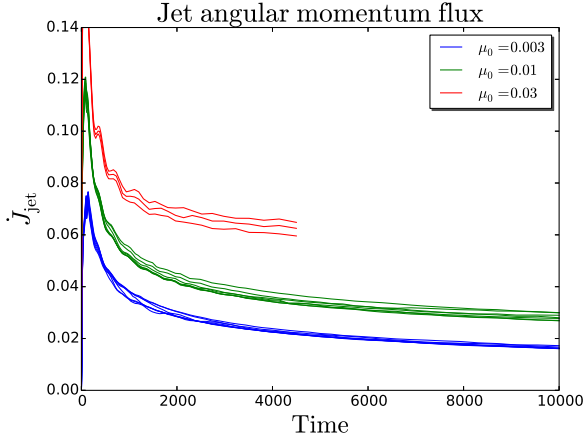


Figure 13. Time evolution of the jet angular momentum flux for the reference type of simulation at radius 10. Simulations with different initial magnetic field form three distinct groups corresponding to $\mu_0 = (0.003, 0.01, 0.03)$ (from down to up)

the terminal speed - for this case the jet accelerates even further out and the asymptotic velocity is not reached at $R = 100$ for low α_m (or highly magnetized) case and is still in a process of transforming the magnetic energy into kinetic. In a follow-up paper we will discuss the terminal jet speed much more detail, demonstrating that already for a moderately weak magnetic field, $\mu \approx 0.05$, the terminal jet speed reaches unity.

In summary, we state that it is the *actual magnetization* in the disk that governs ejection and accretion and that is directly linked to various disk-jet quantities.

4.1. Transport of angular momentum and energy

Here we present the analysis of the angular momentum and energy transport in our simulations. It is common to explore the angular momentum and energy transport by means of their fluxes through a control volume. We define the accretion angular momentum flux $\dot{J}_{\text{acc}} = \dot{J}_{\text{acc,kin}} + \dot{J}_{\text{acc,mag}}$ as the sum of kinetic and magnetic parts, keeping the same control volume as for the mass fluxes (see Appendix B).

Figure 13 shows the time evolution of the jet angular momentum flux for a number of simulations. We divide them in three different groups distinguished by their *initial* magnetization, $\mu_0 = 0.003, 0.01, 0.03$. Different lines within each group represent simulations with different diffusivity parameter α_m . The jet angular momentum flux is calculated through the upper part of the control volume, thus up to $R = 10$.

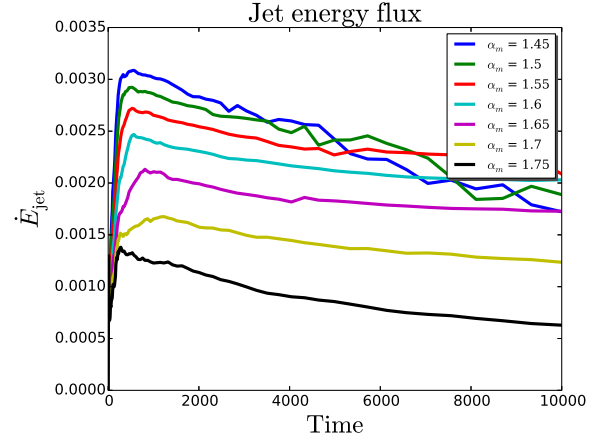


Figure 14. Time evolution of the jet energy flux for the reference type of simulations at radius 10.

As expected, the stronger the overall magnetic field strength is in the disk, the stronger torque it exerts, and thus the higher angular momentum fluxes we find.

Although the magnetic diffusivity parameter α_m differs within each group of lines (marked by different colors), the total torque measured for the corresponding simulations is about the same. This comes from the fact that the total torque is set by the global magnetic field. Thus, the evolution of the total torque is mainly set by the initial conditions.

We note that the simulations applying a strong initial magnetic field (represented by the upper bundle of curves in Figure 13) have been interrupted earlier compared to usual evolution times. For these cases the inner part of the disk became highly magnetized. The strong magnetic field changes the inner disk structure such that our model for the magnetic diffusivity cannot be applied anymore. This is simply because the actual scale height of the disk significantly decreases and does no longer coincide with the initial disk surface. The case of strong magnetic fields we consider as being beyond the scope of this paper. The underlying turbulence might be significantly suppressed as well.

In accordance with previous works (see e.g. Zanni et al. 2007) we find that the ratio of angular momentum extracted by the jet to that provided by the disk accretion is always close to, but slightly larger than unity, $\dot{J}_{\text{jet}}/\dot{J}_{\text{acc}} \gtrsim 1$. The main reason is that the accretion rate in the outer part of the disk is too low to compete with a strong mass loss by the disk wind at these radii.

We define the accretion energy flux (accretion power) as the sum of the mechanical (kinetic and gravitational), magnetic, and thermal energy fluxes,

$$\dot{E}_{\text{acc}} = \dot{E}_{\text{acc,kin}} + \dot{E}_{\text{acc,grv}} + \dot{E}_{\text{acc,mag}} + \dot{E}_{\text{acc,thm}},$$

and, similarly, the jet energy flux (jet power) by

$$\dot{E}_{\text{jet}} = \dot{E}_{\text{jet,kin}} + \dot{E}_{\text{jet,grv}} + \dot{E}_{\text{jet,mag}} + \dot{E}_{\text{jet,thm}}.$$

In contrast to the angular momentum flux, most of the energy flux is being released from the inner part of the disk. This makes the energy flux very sensitive to the conditions in the inner disk. Indeed, Figure 14 shows that the power liberated by the jet strongly depends on the diffusivity parameter, which is the main agent for governing the magnetic field strength. A weaker diffusivity parameter α_m leads to a higher magnetization, and, thus a higher jet power. The same is true for the accretion power.

We further find that the ratio of energy fluxes, namely the ratio of the jet to accretion energy flux, is always close, but slightly lower than unity. This is also in accordance with Zanni et al. (2007).

In this section we have provided some evidence that it is the *actual* magnetization in the disk which governs the fluxes of mass, energy and angular momentum. In the next section we show how exactly these fluxes are connected to magnetization.

4.2. Analysis of magnetization, diffusivity and fluxes

In a steady state, diffusion and advection balance. Advection of the magnetic flux in principle increases the magnetic field strength, predominantly in the inner disk. In contrary, the diffusion smooths out the magnetic field gradient. Therefore, the diffusivity model applied is a key ingredient for these processes, directly influencing the disk structure and evolution.

In the following analysis we will not focus on the profile or the magnitude of the magnetic diffusivity, but concentrate on the resulting magnetization and its time evolution. As discussed above, by changing the magnetic diffusivity parameter α_m we are able to explore how the actual disk magnetization influences various properties of the disk-jet system.

For each parameter run performed, we measure the *actual* physical variables in the disk-jet system, such as the *time-dependent* mean magnetization, accretion fluxes, jet fluxes, or the accretion Mach number. Naturally, the *actual* value of a certain property has evolved from the initial value during the simulation. With mean value we denote the values averaged over a small area of the inner disk,

$$X \equiv \langle X(r, z = 0) \rangle. \quad (27)$$

All mean quantities discussed are averaged over the inner disk midplane from $R = 1.1$ to $R = 1.5$. The choice of the averaging area is motivated as follows. First, in order to avoid any influence of the inner accretion boundary we have moved the inner integration radius about 10 grid cells away from it. Second, we are interested to examine the inner part of the disk, since it is the region where the magnetization is changing predominantly and it is the launching area for the most energetic part of the jet. Third, we want to avoid large magnetic gradients

affecting our averaging area. Although most of jet energy is launched from region broader than this small area, the area is seen as representative. We emphasize that the profiles of the jet power along the disk surface are similar for all simulations. In all cases we investigated, we find that the *general* behaviour of the physical outflow or disk quantities with respect to underlying disk magnetization does not depend on the area where the averaging is done (neither on the location nor on the size).

Keeping all other parameters the same, we have carried out simulations varying the initial magnetization μ_0 and the strength of the magnetic diffusivity α_m . For all our simulations, starting with different initial magnetization, $\mu_0 = 0.003$, $\mu_0 = 0.01$, $\mu_0 = 0.03$, we find that the interrelation between the different jet or disk quantities and the disk magnetization, is essentially the same. We therefore present only one group of simulations, namely that with $\mu_0 = 0.01$. Although the initial magnetic field strength differs, we can already suspect at this point that it is the *actual* rather than the initial strength of the magnetic field in the disk that governs the disk accretion and ejection of the jet, and, thus, playing the major role in the launching process. This has not yet been discussed in the literature so far, as most publication parametrize their simulations by the initial parameters. An exception might be Sheikhezami et al. (2012), who pointed out substantial changes in the disk plasma beta during the time evolution. While the initial magnetization does not play a leading role for the launching process, it is, as was previously shown, responsible for the magnitude of overall torque exerted on the disk.

An interesting representation of the evolution of the main disk-jet quantities are (μ, X) -plots, where X stands for the examining variable. Note, that in these plots the time evolution is hidden.

4.2.1. Accretion Mach number

As it was shown by Königl & Salmeron (2011), there is a link between the mean accretion Mach number and the disk magnetization. In our terms this relation can be expressed as

$$M_{R,\text{act}} = \frac{2}{\sqrt{\gamma}} q \mu_{\text{act}}, \quad (28)$$

where q is the magnetic shear,

$$q = \frac{H J_R}{B_P} = -\frac{B_\phi^+}{B_P}, \quad (29)$$

and where the plus sign denotes a variable estimated on the disk surface. Note that in our case there is no viscous contribution and the factor $1/\sqrt{\gamma}$ appears in the relation since the accretion Mach number is calculated using adiabatic sound speed.

Figure 15 shows that setting q to constant $q = 2\sqrt{\gamma}$ (thus $M_R = 4\mu$) is a good first approximation, especially for the strong magnetization cases. As we will see in the next section, in case of a weak magnetic field the magnetic shear q behaves far from being constant. The closer examination of the magnetic shear q reveals a presence of two different jet launching regimes.

4.2.2. Magnetic shear

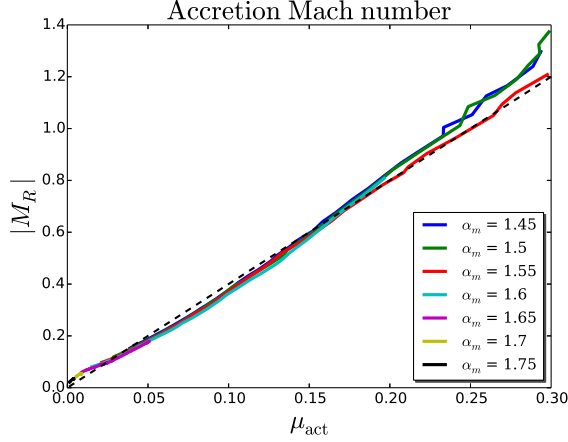


Figure 15. The relation of the accretion Mach number to actual magnetization for the initial magnetization $\mu_0 = 0.01$. The linear approximation $M_R = 4\mu$ is shown by the dashed black line.

A tight relation exists between the magnetic shear q and the ratio between the toroidal and poloidal magnetic field components. We define the magnetic shear q by the radial electric current at the disk midplane, since it does not require to apply the notation of the disk surface, which, in case of a strong magnetic field, might change by up to 40 percent. Note, that the magnetic shear is the first derivative of the accretion Mach number with respect to the magnetization. Therefore it shows the growth rate of the local Mach number or steepness of the curve.

Figure 16 shows the magnetic shear with respect to the underlying inner disk magnetization. We see that the magnetic shear behaves in two different ways - in case of low magnetization, $\mu \leq 0.03 - 0.05$, the magnetic shear is substantially higher in comparison to the case of high magnetization, $\mu \geq 0.03 - 0.05$. The explanation is straightforward: there is a turning point concerning the generation of the toroidal magnetic field versus flux losses through the disk surface (by the outflow). To understand this one needs to set apart the generation processes of the toroidal magnetic field from the loss processes. The rate of the generation of the magnetic field in Keplerian disks is primarily set by the structure of the magnetic field and is rather constant in case of a quasi steady state. On the other hand, the outflow speed (through the disk surface) is highly dependent on the actual disk magnetization. In case of a weak magnetization the outflow speed is rather small, which makes it possible to sustain a stronger magnetic shear. A strong disk magnetization results in a fast outflow, thus setting the maximum limit for the magnetic shear.

4.2.3. Mass and energy flux

The magnetic shear has a great impact on the outflow launching (Ferreira & Pelletier 1995). We confirm this finding by presenting the mass and energy ejection and accretion fluxes.

Figure 17 shows the ratio of the mass ejection rate, $\dot{M}_{ej}(1.5) - \dot{M}_{ej}(1.1)$, to the accretion rate, both averaged over the same area. Obviously, the ejection efficiency is higher for weaker magnetized disks.

This is easy to understand considering Equation 21. In case of a weak magnetic field, the strong magnetic

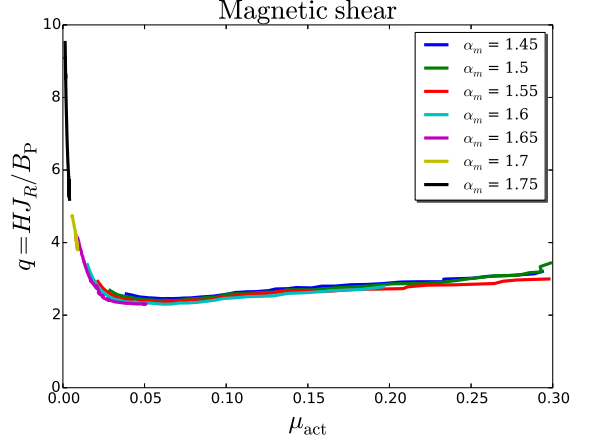


Figure 16. The relation of the magnetic shear with respect to actual magnetization

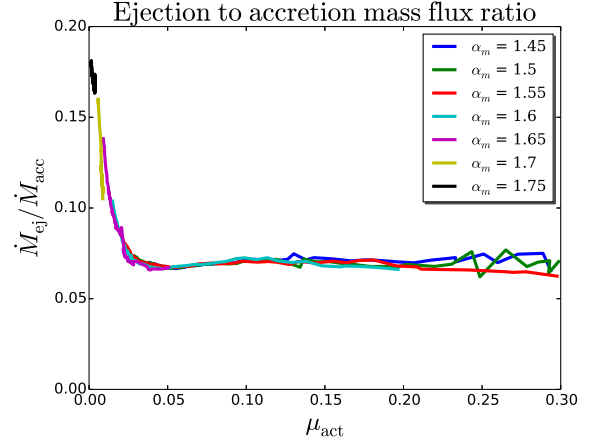


Figure 17. The relation of the mass ejection-to-accretion ratio with respect to actual magnetization

shear (the high toroidal to poloidal magnetic field ratio) leads to faster poloidal acceleration, caused by the force component parallel to the magnetic field. This force also extracts the matter from the disk. In case of a strong disk magnetization, the acceleration of a matter is primarily supported by the centrifugal force.

We note that studying the ejection index (calculated within an area $R = 2 \dots 10$) with respect to the mean disk magnetization leads to very similar results, that is a saturation to values of about 0.35-0.40 in case of a high magnetization and a significant increase in case of a low magnetization.

Figure 18 shows the ratio of the energy ejection density to the average accretion energy, computed in the same way as for the mass fluxes. Compared to the mass fluxes, the energies show the opposite behaviour - the ejection to accretion power is increasing function with magnetization. This is a highly important relation, since it relates two observables. Note that following our findings, there is not a fixed value for the ratio between jet and accretion power. This should be considered when comparing observational results to the theory.

Essentially, this result shows the general importance of the magnetic energy flux compared to the mechanical energy. The mechanical energy flux is always negative, while the magnetic energy flux is positive. In case of a

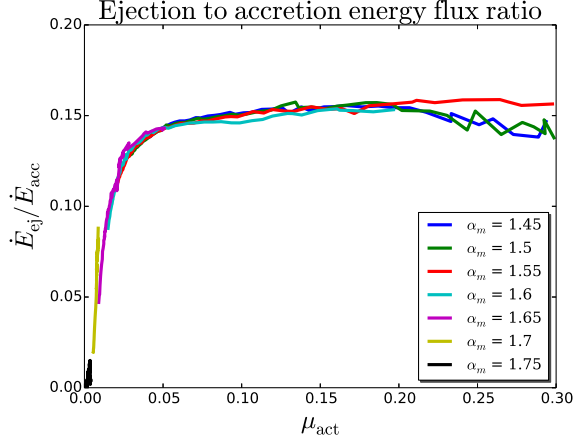


Figure 18. The relation of the energy ejection-to-accretion with respect to actual magnetization

strong magnetic field our results are similar to (Zanni et al. 2007), namely that magnetic energy flux dominating the mechanical flux. We also see a saturation of the flux ratio in case of a moderately strong magnetization. We find that in a weak magnetization case the energy flux ratio can be very small.

We also find that the ejection Mach number, Equation 19, increases almost linearly with magnetization.

Essentially, the *general* behaviour of the mass and energy flux ratios does depend on the averaging area or its position.

The accretion power (see Appendix, Equation B3) is mainly determined by the accretion rate at the inner disk radius. Assuming a typical scale height for the mass accretion as ϵr , the accretion power can be estimated considering the magnetic shear and the actual magnetization of the disk,

$$\dot{E}_{acc} \simeq 0.06 q \mu_{act} \dot{E}_0, \quad (30)$$

where \dot{E}_0 is the unit power (see Appendix A).

In case of strongly magnetized disks one can assume that the magnetic shear is approximately constant $q \approx 3$, and this relation transforms into $\dot{E}_{acc} \simeq 0.2 \mu_{act} \dot{E}_0$. Note that this result connects two essential quantities - the accretion power which manifests itself by the accretion luminosity to the disk magnetization, which is intrinsically hidden from the observations.

5. A STABLE LONG-TERM EVOLUTION

In this section we discuss the commonly used diffusivity model and the reasons why we think that it fails in case of very long-term simulations, in particular when treating weakly magnetized disks. In order to overcome this problem - the accretion instability - we propose another magnetic diffusivity model. This new model enables us to simulate the evolution of the disk-jet system for much longer times.

5.1. Constraints on the diffusivity parameters

The simple idea that the induction of the magnetic flux in steady state is compensated by the flux losses, both by diffusion and magnetic flux escape through the disk surface, becomes hardly applicable in case of a weak magnetic field. As discussed previously (see Section 2.5),

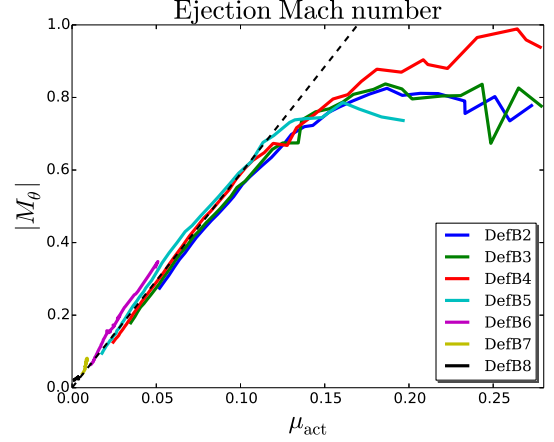


Figure 19. The relation of the ejection Mach number with respect to actual magnetization. The slope of dashed line $\beta = 5.9$.

in order to keep the magnetic field distribution properly bent, the magnetic diffusivity parameter α_m must be linked to the anisotropy parameter χ . Equation 20 was obtained considering the standard magnetic diffusivity model. A more general relation can be derived assuming a curvature of the magnetic field of about 0.5, that is the mean curvature of the initial field distribution (see Equation 9),

$$(\alpha_{ssm} \chi - M_\theta) \alpha_{ssm} \leq \mu. \quad (31)$$

Solving this inequality for α_{ssm} and assuming $M_\theta \propto \beta \mu$, we find

$$\alpha_{ssm} \leq \alpha_0 = \frac{\beta}{2} \mu_\chi + \sqrt{\left(\frac{\beta}{2}\right)^2 \mu_\chi^2 + \mu_\chi}, \quad (32)$$

where $\mu_\chi = \mu/\chi$, and $\beta \approx 6$ in our simulations. This relation shows that in order to keep the disk magnetic field properly bent, the α_{ssm} should behave differently in the two limits of magnetization. A linear relation to the magnetization in case of a strong magnetic field, and proportional to the square root of magnetization in case of a weak field. In case of a strong deviation from this relation, the magnetic field structure will be substantially affected, resulting in a high field inclination (for $\alpha_{ssm} \ll \alpha_0$), or a strong outward bending (for $\alpha_{ssm} \gg \alpha_0$).

For equation 32 we have implicitly assumed a linear relation between the ejection Mach number (at the disk surface) and the magnetization. In fact our simulations approve such an interrelation. Figure 17 shows that for a moderately strong magnetic field, there is a linear relation between the ejection Mach number and underlying disk magnetization. This behaviour is also consistent with ejection to accretion mass flux ratio we have discussed above.

As a consequence of Equation 16, the α_{ssm} plays a direct role in determining the strength of the poloidal electric current with respect to the toroidal current. We find in our simulations that in order to sustain jets, the ratio of the poloidal to the toroidal current should be sufficiently high (about 15).

The difficulty in performing simulations of weakly magnetized outflows is that the specific torques may *increase* towards the disk surface area, just because of the low densities over there. This will lead to a layered accretion

along the disk surface, and, thus, much lower accretion along the midplane. Although this might be a relevant process in reality, our numerical setup is not suited for the treatment of such a configuration.

The standard, commonly used magnetic diffusivity model is parametrized by two constants, α_m and χ . In general, choosing a high anisotropy parameter χ implies a low diffusivity parameter α_m . Together, this will lead to a decrease in the poloidal electric current and an increase in the toroidal current (see Equation 16). Thus, the resulting torque will not be sufficient to brake the dense matter along the midplane, and will lead to layered accretion. An anisotropy parameter lower than unity has proven to lead to a smoother time evolution, since it allows for stronger poloidal currents at the midplane, and, thus, a mass accretion which is developed over the full disk height. Another option to have $\chi > 1$ would be to modify the vertical diffusivity profile such that it reaches the maximum not at the disk midplane, but at the disk surface. This would also help to develop a strong electric current in the disk midplane.

5.2. The accretion instability

Here, we discuss another problem, which the standard diffusivity model is prone to. As previously shown, most of the simulations suffer from the mass loss from the disk, leading to the increase of the magnetization. However, the increase of the magnetization further amplifies the mass loss. This is known as the accretion instability, first studied by Lubow et al. (1994), and later confirmed for more general cases (Campbell 2009). If, on the other hand, the diffusivity is too high (chosen by a high α_m parameter), inevitable diffusion of the magnetic field will lead to the situation that a jet cannot be sustained anymore.

We like to emphasize that the main reason for the increase of magnetization is the mass loss, but not the actual magnetic field amplification. This is a direct consequence of the accretion instability, namely, a lack of sufficient feedback that could bring the accretion system back to a stable state. In other words, in order to run long-term simulations one needs to apply a diffusivity model that provides a stronger feedback to the diffusivity profile than the standard choice $\propto \sqrt{2\mu}$.

5.3. A proper magnetization profile

The direct consequence of the accretion instability is that the magnetization increases towards the center. It is easy to show that the behaviour of the magnetization has to be opposite. In accretion disks producing outflows, the mass accretion rate must naturally increase with radius. Assuming a radial self-similarity of the disk and taking into account that the accretion Mach number is linearly related to the magnetization and that $\rho \propto C_s^3$, one derives

$$\beta_\mu = \xi - 2 - 4\beta_{C_s}, \quad (33)$$

where ξ is the ejection index and β_X represent the power law index of a physical quantity X . Considering that magnetized disks are very efficient in producing outflows, $\xi \approx 0.2 - 0.4$, one may expect β_μ to be positive (if $\beta_{C_s} \approx -1/2$), thus, an increasing function with radius. However, the disk structure itself can be re-arranged such

that $|\beta_{C_s}| \leq 1/2$, that eventually will satisfy the relation 33. This is indeed what we find.

One should, however, keep in mind that this equation is a rough estimate and might be subject to the different disk physics involved. If the magnetic torque is not the only supporter of the accretion as in case of viscous simulations of Murphy et al. (2010) the above presented relation might be relaxed. However, the similar analysis can be performed to set the limit of the magnetization with respect to other quantities.

5.4. A modified diffusivity model

In this section we present a diffusivity model, which does not suffer from the accretion instability. Although the standard diffusivity model gave us an opportunity to probe a wider parameter space, it is not applicable for very long-term studies.

We emphasize that the transition from the a direct simulation of turbulence to the mean field approach, which lacks the small scales by design, is indeed subtle. So far, in the literature, the jet launching problem is addressed without considering the origin of the magnetic field by a dynamo. Therefore, the only way of amplifying the magnetic field is by advection (or stretching in case of a toroidal field). There is also no intrinsic angular momentum transport by the turbulence itself. The only term we need to model when applying a small scale turbulence, is the effective magnetic diffusivity. This might have surprising consequences. In order to suppress the turbulence, one should rather *amplify* the effective diffusivity - leading to a stronger decay of the magnetic field and resembling the quenching of diffusivity (or dynamo) - rather than decrease it - leading to stronger advection and thus an amplification of the magnetic field. The main motivation of our new model for the diffusivity - is to consider stronger feedback by the disk magnetization. We overcome the accretion instability by assuming a stronger dependence of α_{ssm} on the magnetization,

$$\alpha_{ssm} = \alpha_m \sqrt{2\mu_0} \left(\frac{\mu}{\mu_0} \right)^2, \quad (34)$$

where we choose $\alpha_m = 1.55$ and $\mu_0 = 0.01$. Here we keep the previous overall form and constants, indicating that both models are the same at the magnetization μ_0 . A quadratic dependence on μ was chosen in order to amplify the feedback. Choosing a lower power than two might have revealed other complications, for example a feedback too weak to work fast enough, and keep α_{ssm} under the constraint of Equation 32. We will refer to this diffusivity model as *strong diffusivity model*.

5.5. The long-term disk-outflow evolution

Applying our strong diffusivity model enables us to overcome the accretion instability. As a result, we were able to perform our simulations for *much* longer times, reaching evolutionary time steps of $t > 150,000$ which corresponds to approximately 25,000 revolutions at the inner disk orbit.

Figure 20 shows the typical computation domain and the initial dynamics of the system. As usual, the evolution starts with the propagation of the toroidal Alfvén wave, resulting in a propagating cocoon. At this point, the innermost area ($R \leq 10$) has reached a quasi steady

state, while the outer part has not even slightly moved from the initial state. Figure 21 presents the same simulation at a later state when a strong outflow has been developed. Notice the difference between the inner part, $r \leq 200$ and the outer part, $r \geq 200$. The inner part has already relaxed to a steady state, while the outer region shows rapid accretion and ejection patterns. This is a direct consequence of the new diffusivity model. The logic behind implementing the enhanced feedback is valid only when the accumulation of the flux is possible. The initial imbalance between advection and diffusion in the outer part leads to a rapid advection of the magnetic flux to the inner disk. As a result, the rapid accretion further leads to higher inclination angles of the magnetic field (smaller angle with respect to the disk surface). This results in a higher efficiency for the toroidal magnetic field induction, thus leading to even more rapid accretion and ejection.

Figure 22 shows a long term evolution on a small sub-grid of the simulation with our strong diffusivity model. As can be seen, until time $t = 10,000$ only a small fraction of the disk has dynamically evolved (up to $R \approx 50$), while at later times also the outer parts of the disk do reach a new dynamic state. A steady outflow establishes from the whole disk surface (shown on this sub-grid), and reaches super-fast magnetosonic speed. Note that the positions of the critical MHD surfaces are constant in time, which is a further signature of a steady state.

The outflow reaches maximum velocities typically of the order of 100 km s^{-1} for YSO, or $70,000 \text{ km s}^{-1}$ in case of AGN. Concerning observationally relevant scales, our simulations compare to the following numbers. Our numerical grid is comparable to 150 AU for YSO, and 0.14 pc in case of AGN. Physically more meaningful is the grid size where our simulation has reached a steady state. That is a size comparable to 25 AU for YSO, and 5000 AU in case of AGN, but can be extended by running the simulations longer. The dynamical time scale of 150,000 time units (or 25,000 disk orbits) corresponds to about 550 years in case of YSO and about 200 years in case of AGN. Typical accretion rates of our simulations are $3 \times 10^{-7} M_{\odot} \text{ yr}^{-1}$ for YSO, and $0.1 M_{\odot} \text{ yr}^{-1}$ in case of AGN, but one has to keep in mind that these values depend not only on the intrinsic scaling of central mass and inner disk radius, but also on the scaling of density. Therefore, we herewith present the most extended and longest MHD simulations of jet launching obtained so far - connecting the jet launching area close to the central object with the asymptotic domain which is accessible by observations.

Although a spherical grid is computationally very efficient and may allow to extend the computational domain to almost any radius, in reality its application for the jet launching simulations is somewhat limited. There are two reasons for that. First, it takes obviously much longer time for the outer disk areas to evolve into a new dynamical steady state. Thus, outer disk will remain close to the initial state of the simulation for quite some time. Second, and a more severe drawback is the lack of resolution for the asymptotic jet. For example, for distances $R > 500 R_0$ along the rotational axis, the jet radius of about $r_{\text{jet}} \approx 25$ can be resolved only by about 5 grid cells (applying our typical resolution). We therefore restrict our computational domain for such grid size

to about $R_{\text{out}} \simeq 1000 - 2000 R_0$. The above mentioned resolution issue is in fact one of the advantages for using cylindrical coordinates for jet formation simulations.

5.6. Results of the strong diffusivity model

By design, the purpose of our strong diffusivity model was to avoid the accretion instability. As a consequence of this application, magnetization profile does not decrease with radius (see Figure 23). Although both simulations (with standard and strong diffusivity model) start from the same initial disk magnetization, the disk evolution results in a quite different magnetization distribution. The standard diffusivity model (our reference simulation from above) results in a magnetization profile decreasing with radius. In contrast, for the strong diffusivity model a rather flat magnetization profile emerges. In non-viscous simulations, assuming radial self-similarity, a flat (or not decreasing with radius) profile is essential for sustaining a continuous accretion flow at any given radius.

As soon as a steady state is reached, the evolutionary track for this simulation is represented by a simple dot in all (μ, X) -diagrams (at least from 1000 to 150,000 time units). The mean inner disk magnetization is $\mu \approx 0.012$. We find that this simulation fits to every relation presented above, such as mass and energy flux ratios, or magnetic shear, that were derived applied a standard diffusivity model. In other words, the aforementioned dots belong to the curves drawn in the (μ, X) -diagrams.

There are several distinct features one can derive from the resulting magnetic field structure. Figure 24 shows the toroidal to poloidal magnetic field component ratio. Taking into account that the disk magnetization (calculated from poloidal component only) is uniform, three different regions can be distinguished. The first region is between the midplane and the disk surface where the toroidal magnetic field reaches its maximum and the torques change sign. The second region is between the disk surface and the Alfvén surface where the ratio of the field components is quite constant. The third region is beyond the Alfvén surface when the poloidal component of the magnetic field becoming weak enough to keep a rigid magnetic field structure and toroidal component starts to dominate the poloidal one.

5.7. Dynamical profiles of a steady state accretion disk

In this subsection we further explore the disk structure in a steady state. In Figure 25 we present the radial profiles of certain magnetohydrodynamical variables along the midplane. We show the profiles derived from our numerical simulations with their approximations by power laws, and compare them to the initial distribution. These radial profiles are obtained along the disk midplane, however, they also hold at least for one disk semi-height. The thetoidal profiles that normalized to the corresponding midplane value (not shown here) almost coincide with each other, indicating that the assumption of a self-similar disk is in fact reasonable, though different power indexes should be used.

In particular, Figure 25 shows how the disk structure evolves from a certain initial power law distribution into another power law profile. We see distinct power law profiles for radii up to $R \leq 250$. This corresponds to

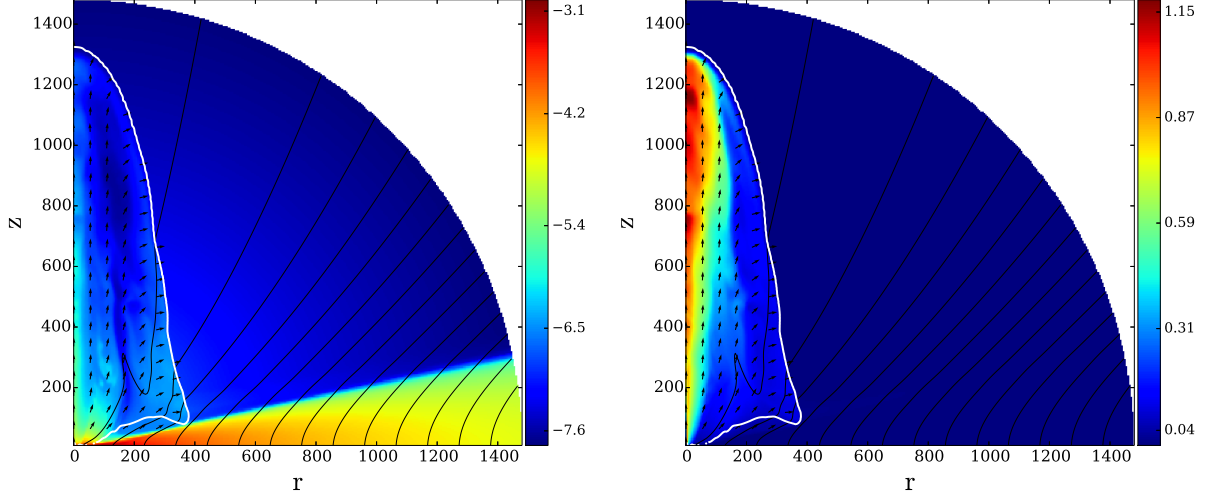


Figure 20. Initial evolution of the strong diffusivity setup at $T = 1500$. Colors represent the logarithm of density (left) and speed (right), black lines denote the magnetic field, arrows the normalized velocity, and white line shows the Alfvén surface. Arrows show normalized velocity vectors.

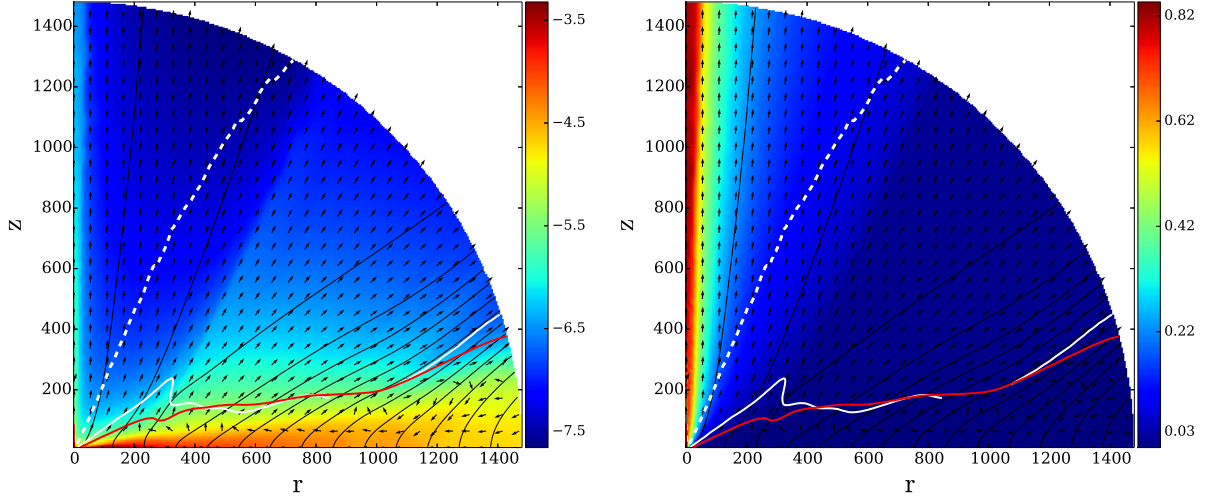


Figure 21. Time snapshot of the strong diffusivity setup at $T = 150,000$. Shown is the density (colors, in logarithmic scale), the poloidal magnetic flux (thin black lines), the sonic (red line), Alfvén (white line), and fast magnetosonic (white dashed line) surfaces. Arrows show normalized velocity vectors.

the area where the disk evolution has reached a steady state. For very small radii $R \leq 1.1$ we also see a deviation from a power law profile, that we consider as a boundary effect.

At time $t = 150,000$, we find the following numerical values for the power law coefficients β_X for the different variables at the midplane $X(r, \theta = \pi/2) \sim r^{\beta_X}$. The disk rotation remains Keplerian throughout the whole time evolution, thus $\beta_{V_\phi} = -1/2$. The radial profiles for density and gas pressure slightly change from their initial distribution. The density power law index changes from $\beta_\rho = -3/2$ to $\beta_\rho = -4/3$, while for the pressure it changes from $\beta_P = -5/2$ to $\beta_P = -20/9$. For the accretion velocity we find a profile of $\beta_{V_R} = -2/5$, and $\beta_{B_\theta} = -10/9$ for the magnetic field. As a consequence, the profile for the magnetization remains about constant $\beta_\mu \sim 2\beta_{B_\theta}/\beta_P = (-20/9)/(20/9)$. The accretion velocity remains subsonic over the whole disk with an accretion Mach number of $V_R/C_s \approx 0.1$.

Following Ferreira & Pelletier (1995) and considering

the mass accretion $\dot{M}_{\text{acc}} \sim R^2 \rho V_R$ it is easy to get the ejection index $\xi = 0.26$. This is in accordance with previous work Sheikhnezhani et al. (2012).

5.8. Discussion of the new diffusivity model

Our strong diffusivity model, Equation 34, does not *necessarily* lead to a flat magnetization profile. The model does not directly force the magnetization to be uniformly distributed - in opposite, the profile is expected to be outwardly increasing. As we previously showed the magnetization profile is linked to the ejection index and it has to be positive if the sound speed stays as initially distributed. What we found is that the disk hydrodynamics changes such that the magnetization of the disk remains flat, thus satisfying Equation 33.

Another way of reasoning is the following. In case of a flat magnetization profile the result of the simulation is not sensitive to the diffusivity model anymore. In other words, it is possible to switch back from the new diffusivity model to the standard model when the radial mag-

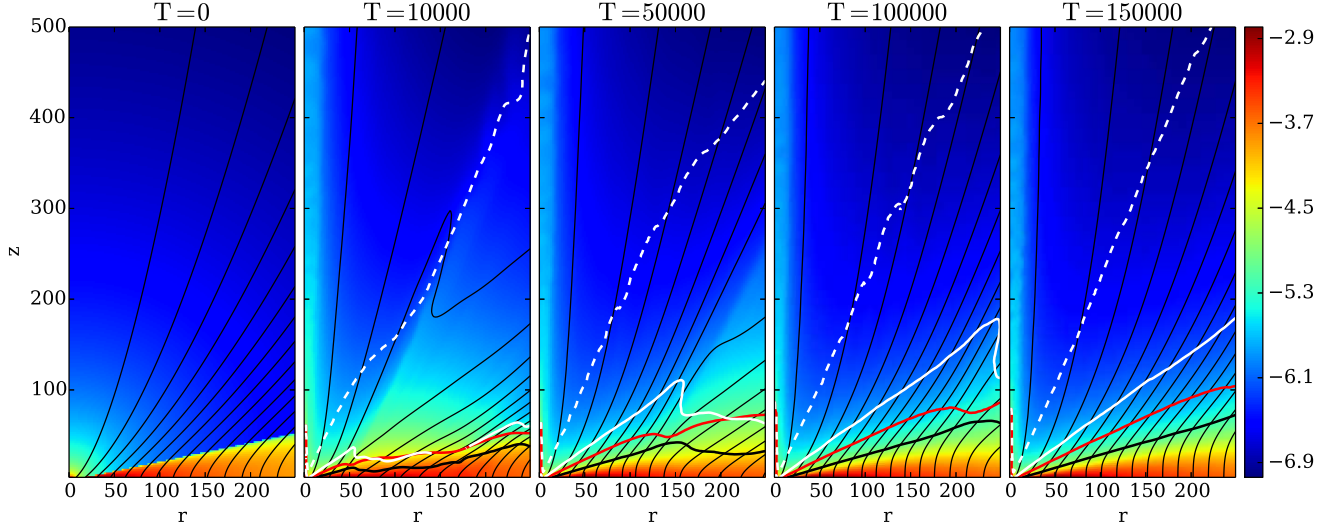


Figure 22. Time evolution of the disk-jet structure for the strong diffusivity simulation. Shown is the evolution of density (colors, in logarithmic scale), the poloidal magnetic flux (thin black lines), the disk surface (thick black line) the sonic (red line), Alfvén (white line), and fast magnetosonic (white dashed line) surfaces.

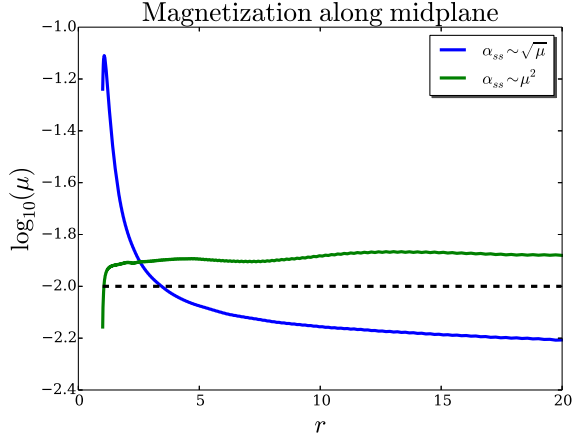


Figure 23. Magnetization distribution throughout the disk for reference and strong diffusivity model at $T=10,000$. The dashed line marks the initial magnetization.

netization profile is uniform (along the midplane). However, the diffusivity parameter α_m has to be correspondingly re-normalized. The only substantial deviation from a uniform profile is in the innermost disk, which might be influenced by the boundary condition. In fact, we performed such a test simulation, switching back from strong diffusivity to standard diffusivity model. As expected, the accretion instability starts to manifest itself similarly as before, leading to the typical magnetization profile (increasing towards the center). However, it takes much longer time to substantially affect the outer parts of the disk.

The steady state solution achieved when using our strong diffusivity model, perfectly fits to the results obtained by the standard model (shown previously as a dot on the plots). This actually approves our understanding that the main agent in driving outflows is the *actual* magnetization, and that the magnetic diffusivity is only the *mediator* through which the magnetic field structure is being governed. A self-consistent treatment of turbulence is not feasible yet in the context of outflow launch-

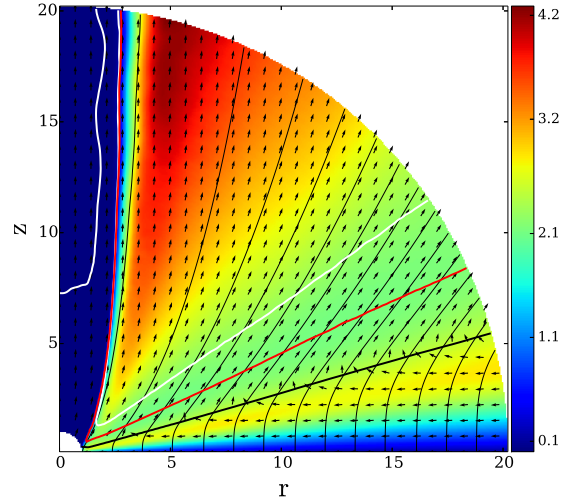


Figure 24. The ratio of the toroidal to poloidal magnetic field for the strong diffusivity model at $T = 10,000$. Lines represent the disk (thick black line) the sonic (red line), the Alfvén (white line) surfaces. Arrows show normalized velocity vectors.

ing. Therefore, what should be considered at first place, is the resulting magnetic field strength and distribution, but not the diffusivity model itself.

6. CONCLUSIONS

We have presented results of MHD simulations investigating the launching of jets and outflows from a magnetically diffusive accretion disk. The time evolution of the disk structure is self-consistently taken into account. The simulations are performed in axisymmetry applying the MHD code PLUTO 4.0. In contrast to previous work we have applied a *spherical* coordinate system and numerical grid, which implies substantial benefits concerning the numerical resolution and the stability (in time evolution) of the simulations.

In particular, we have obtained the following results.

(1) Our numerical setup in spherical coordinates for disk-jet related problems is very robust. The use of

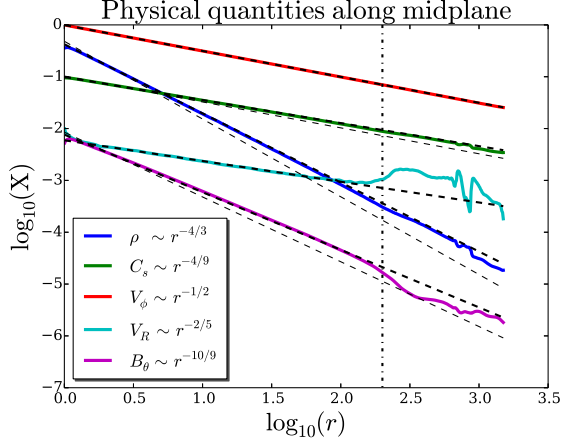


Figure 25. Physical quantities along the midplane for the strong diffusivity model. Colors show different variable profile, thick dashed lines correspond to certain power law, the mismatched thin dashed lines correspond to initial distributions of variables. Vertical dashed line marks $r = 200$.

spherical geometry in the context of the outflow launching cannot be underestimated. It allows to study the launching of outflows for very long time (more than 150,000 time units) on highly resolved (up to 24 cells per disk height) and at the same time very large ($1500 r_0$) domains. On the other hand, a spherical grid somewhat limits the study of jet propagation, since the resolution far from the origin becomes low. The rather low resolution in the outer disk region, where the dynamical timescales are long, helps to smooth out small-scale disturbances, thus helping in establishing a steady state.

(2) Our study has approved a robust disk-outflow structure, however for the highest resolution the evolution is prone to have some more fluctuations. The ability to evolve the disk for very long time disentangles the complex interrelations between the essential quantities for the jet launching. Those are the disk actual magnetization (at a certain time and averaged for a certain location), the mass, energy and angular momentum fluxes, and the jet terminal velocity.

(3) Our main result is that it is the *actual* rather than the initial disk magnetization that plays a key role for the jet formation and directly affects the accretion power. The value of the *initial* magnetization can fail to properly characterize the disk-jet properties, but sets the overall jet torque and the disk's magnetic reservoir. This becomes obvious for very weakly magnetized disks ($\mu_0 = 0.003$). In this case, when choosing a low magnetic diffusivity, the magnetic flux can still be accumulated to a high magnetization in the inner disk. We find that the actual magnetization necessary for sustaining a stable jet is of order of 10^{-3} , in accordance with Murphy et al. (2010).

(4) We showed that the ejection Mach number in case of moderately strong magnetization ($\mu < 0.15$) is linearly

related with respect to the disk magnetization. This is indeed consistent with the linear to magnetization mass ejection to accretion relation. The mass ejection index (the ratio between ejection and accretion) is about 0.3 and thus similar to the literature values.

(5) We found that in case of uniform magnetization, the MHD disk quantities show a self-similar structure, i.e. resulting in approximately the same vertical profile, and a radial power law distribution. In case of the strong diffusivity model we have presented the corresponding power law indices for all MHD quantities, although we believe that these power law indices may directly depend on the actual strength of the magnetization. This would be a natural consequence of the ejection index being a function of magnetization as well.

(6) We showed that there are two principally different regimes for outflow launching, complementary to each other. In case of weak magnetic fields (below $\mu \approx 0.03$) we see signatures of a strong magnetic shear, which results in less powerful, but more efficient (higher ejection index) outflows. In case of a higher magnetization, the magnetic shear, the ejection efficiency and the energy ejection to accretion flux ratio do not strongly depend on the magnetization

(7) We found the upper theoretical limit for the parameter specifying the anisotropy χ in the magnetic diffusivity in case of the standard diffusivity model, essentially depending on the actual magnetization in the disk. In the limit of low magnetization the anisotropy parameter must satisfy $\chi \leq 1/\alpha_m^2$.

(8) We showed that in non-viscous steady state, assuming radial self-similarity, the magnetization profile should be non-decreasing function of radius. In steady state, jet launching disks must have a radially increasing profile of the mass accretion rate. This is a requirement of a positive ejection index. Taking into account that i) the accretion Mach number is proportional to the magnetization and ii) assuming that the radial profile of the sound speed does not strongly deviate from Keplerian, we showed that the index of the magnetization profile is non-negative.

This is paper I in a series of papers, that studies the long term evolution of outflow-generating disks. In two follow-up papers we will present the i) connection of the jet properties (the potential observables) with the underlying disk quantities, and we will ii) extend the present setup to simulations including a disk magnetic field that is self-generated by a mean-field dynamo.

We thank Andrea Mignone and the PLUTO team for the possibility to use their code. We appreciate many helpful discussions with Andrea Mignone and also competent suggestions by the unknown referee. The simulations were performed on the THEO cluster of Max Planck Institute for Astronomy. This work was partly financed by the SFB 881 of the German science foundation DFG.

APPENDIX

UNITS AND NORMALIZATION

Here we write up the typical normalization to be used to apply our code units to different astrophysical jet-launching objects, such as young stellar objects (YSO), and active galactic nuclei (AGN). The main normalization units are the Keplerian speed at the inner disk radius,

$$V_{K0} = 94 \text{ km s}^{-1} \left(\frac{M}{M_{\odot}} \right)^{1/2} \left(\frac{R_0}{0.1 \text{ AU}} \right)^{-1/2} = 6.7 \times 10^4 \text{ km s}^{-1} \left(\frac{R_0}{10 R_S} \right)^{-1/2}$$

the time unit that is expressed in units of $T_0 \equiv R_0/V_{K0}$,

$$T_0 = 1.7 \text{ days} \left(\frac{M}{M_{\odot}} \right)^{-1/2} \left(\frac{R_0}{0.1 \text{ AU}} \right)^{3/2} = 0.5 \text{ days} \left(\frac{R_0}{10 R_S} \right)^{3/2}$$

The mass accretion rate is a parameter which is in principle accessible by observation. Thus, the normalization of density ρ_0 can be chosen by setting suitable accretion rates $\dot{M}_0 = R_0^2 \rho_0 V_{K0}$. Assuming $\dot{M}_{\text{acc}} \simeq 10^{-7} M_{\odot} \text{ yr}^{-1}$, $\dot{M}_{\text{acc}} \simeq 10 M_{\odot} \text{ yr}^{-1}$, and taking into account that the typical accretion rates our simulations provide are of order of $\dot{M}_{\text{acc}} \simeq 0.01$ (in code units), one gets

$$\dot{M}_0 = 3 \times 10^{-5} M_{\odot} \text{ yr}^{-1} \left(\frac{\rho_0}{10^{-10} \frac{\text{g}}{\text{cm}^3}} \right) \left(\frac{M}{M_{\odot}} \right)^{1/2} \left(\frac{R_0}{0.1 \text{ AU}} \right)^{3/2} = 10 M_{\odot} \text{ yr}^{-1} \left(\frac{\rho_0}{10^{-12} \frac{\text{g}}{\text{cm}^3}} \right) \left(\frac{M}{10^8 M_{\odot}} \right)^{1/2} \left(\frac{R_0}{10 R_S} \right)^{3/2}$$

The torque and power are given in units of $\dot{J}_0 = R_0^3 \rho_0 V_{K0}^2$ and $\dot{E}_0 = R_0^2 \rho_0 V_{K0}^3$ respectively,

$$\begin{aligned} \dot{J}_0 &= 3.0 \times 10^{36} \text{ dyne cm} \left(\frac{\rho_0}{10^{-10} \frac{\text{g}}{\text{cm}^3}} \right) \left(\frac{M}{M_{\odot}} \right) \left(\frac{R_0}{0.1 \text{ AU}} \right)^2 = 1.2 \times 10^{51} \text{ dyne cm} \left(\frac{\rho_0}{10^{-12} \frac{\text{g}}{\text{cm}^3}} \right) \left(\frac{M}{10^8 M_{\odot}} \right)^3 \left(\frac{R_0}{10 R_S} \right)^2 \\ \dot{E}_0 &= 1.9 \times 10^{35} \text{ erg s}^{-1} \left(\frac{\rho_0}{10^{-10} \frac{\text{g}}{\text{cm}^3}} \right) \left(\frac{M}{M_{\odot}} \right)^{3/2} \left(\frac{R_0}{0.1 \text{ AU}} \right)^{1/2} = 2.6 \times 10^{46} \text{ erg s}^{-1} \left(\frac{\rho_0}{10^{-12} \frac{\text{g}}{\text{cm}^3}} \right) \left(\frac{M}{10^8 M_{\odot}} \right)^2 \left(\frac{R_0}{10 R_S} \right)^{1/2} \end{aligned}$$

The magnetic field is normalized to its values at the midplane, $B_0 = \sqrt{8\pi P_0 \mu}$,

$$\begin{aligned} B_0 &= 15 \text{ G} \left(\frac{\mu}{0.1} \right)^{1/2} \left(\frac{\epsilon}{0.1} \right) \left(\frac{\rho_0}{10^{-10} \frac{\text{g}}{\text{cm}^3}} \right)^{1/2} \left(\frac{M}{M_{\odot}} \right)^{1/2} \left(\frac{R_0}{0.1 \text{ AU}} \right)^{-1/2} \\ &= 1 \text{ kG} \left(\frac{\mu}{0.1} \right)^{1/2} \left(\frac{\epsilon}{0.1} \right) \left(\frac{\rho_0}{10^{-12} \frac{\text{g}}{\text{cm}^3}} \right)^{1/2} \left(\frac{M}{10^8 M_{\odot}} \right)^{1/2} \left(\frac{R_0}{10 R_S} \right)^{-1/2} \end{aligned}$$

CONTROL VOLUMES AND THE FLUXES IN DISK AND JET

For the fluxes of energy and angular momentum, we keep the same notation as for the mass flux,

$$\dot{J}_{\text{acc,kin}} = -2 \int_{S_1}^{S_R} r \rho V_{\phi} \mathbf{V}_p \cdot d\mathbf{S}, \quad \dot{J}_{\text{acc,mag}} = 2 \int_{S_1}^{S_R} r B_{\phi} \mathbf{B}_p \cdot d\mathbf{S}. \quad (\text{B1})$$

We define the jet angular momentum flux $\dot{J}_{\text{jet}} = \dot{J}_{\text{jet,kin}} + \dot{J}_{\text{jet,mag}}$ with

$$\dot{J}_{\text{jet,kin}} = -2 \int_{S_S} r \rho V_{\phi} \mathbf{V}_p \cdot d\mathbf{S}, \quad \dot{J}_{\text{jet,mag}} = 2 \int_{S_S} r B_{\phi} \mathbf{B} \cdot d\mathbf{S}. \quad (\text{B2})$$

Similarly, we define the accretion power $\dot{E}_{\text{acc}} = \dot{E}_{\text{acc,mec}} + \dot{E}_{\text{acc,mag}} + \dot{E}_{\text{acc,thm}}$ as the sum of the mechanic, magnetic, and thermal energies,

$$\dot{E}_{\text{acc,mec}} = -2 \int_{S_1}^{S_R} \left(\frac{\mathbf{V}^2}{2} + \Phi_g \right) \rho \mathbf{V}_p \cdot d\mathbf{S}, \quad \dot{E}_{\text{acc,mag}} = -2 \int_{S_1}^{S_R} \mathbf{E} \times \mathbf{B} \cdot d\mathbf{S}, \quad \dot{E}_{\text{acc,thm}} = -2 \int_{S_1}^{S_R} \frac{\gamma}{\gamma - 1} P \mathbf{V}_p \cdot d\mathbf{S}, \quad (\text{B3})$$

and the jet power $\dot{E}_{\text{jet}} = \dot{E}_{\text{jet,kin}} + \dot{E}_{\text{jet,grv}} + \dot{E}_{\text{jet,mag}} + \dot{E}_{\text{jet,thm}}$ with

$$\dot{E}_{\text{jet,kin}} = -2 \int_{S_S} \frac{\mathbf{V}^2}{2} \rho \mathbf{V}_p \cdot d\mathbf{S}, \quad \dot{E}_{\text{jet,grv}} = -2 \int_{S_S} \Phi_g \rho \mathbf{V}_p \cdot d\mathbf{S}, \quad (\text{B4})$$

$$\dot{E}_{\text{jet,mag}} = -2 \int_{S_S} \mathbf{E} \times \mathbf{B} \cdot d\mathbf{S}, \quad \dot{E}_{\text{jet,thm}} = -2 \int_{S_S} \frac{\gamma}{\gamma - 1} P \mathbf{V}_p \cdot d\mathbf{S}. \quad (\text{B5})$$

REFERENCES

- Bai, X.-N. & Stone, J. M. 2013, ApJ, 767, 30
 Balbus, S. A. & Hawley, J. F. 1991, ApJ, 376, 214

- Banerjee, R., Klessen, R. S., & Fendt, C. 2007, *ApJ*, 668, 1028
- Beckwith, K., Armitage, P. J., & Simon, J. B. 2011, *MNRAS*, 416, 361
- Blandford, R. D. & Payne, D. G. 1982, *MNRAS*, 199, 883
- Cabrit, S., Edwards, S., Strom, S. E., & Strom, K. M. 1990, *ApJ*, 354, 687
- Camenzind, M. 1990, in *Reviews in Modern Astronomy*, Vol. 3, Reviews in Modern Astronomy, ed. G. Klare, 234–265
- Campbell, C. G. 2009, *MNRAS*, 392, 271
- Casse, F. & Ferreira, J. 2000, *A&A*, 353, 1115
- Casse, F. & Keppens, R. 2002, *ApJ*, 581, 988
- . 2004, *ApJ*, 601, 90
- Colella, P. & Woodward, P. R. 1984, *Journal of Computational Physics*, 54, 174
- Fendt, C. & Sheikhnezami, S. 2013, *ApJ*, 774, 12
- Ferreira, J. 1997, *A&A*, 319, 340
- Ferreira, J. & Casse, F. 2013, *MNRAS*, 428, 307
- Ferreira, J. & Pelletier, G. 1995, *A&A*, 295, 807
- Fromang, S. 2013, in *EAS Publications Series*, Vol. 62, EAS Publications Series, 95–142
- Gaibler, V., Khochfar, S., Krause, M., & Silk, J. 2012, *MNRAS*, 425, 438
- Goedbloed, J. P., Beliën, A. J. C., Holst, B. V. D., & Keppens, R. 2004, *Physics of Plasmas*, 11, 4332
- Gressel, O. 2010, *MNRAS*, 405, 41
- Hawley, J. F., Gammie, C. F., & Balbus, S. A. 1995, *ApJ*, 440, 742
- Johansen, A. & Levin, Y. 2008, *A&A*, 490, 501
- Keppens, R., Casse, F., & Goedbloed, J. P. 2002, *ApJ*, 569, L121
- King, A. R., Pringle, J. E., & Livio, M. 2007, *MNRAS*, 376, 1740
- Königl, A. & Salmeron, R. The Effects of Large-Scale Magnetic Fields on Disk Formation and Evolution, ed. Garcia, P. J. V., 283–352
- Lesur, G. & Longaretti, P.-Y. 2009, *A&A*, 504, 309
- Li, Z. 1995, *ApJ*, 444, 848
- Londrillo, P. & del Zanna, L. 2004, *Journal of Computational Physics*, 195, 17
- Lubow, S. H., Papaloizou, J. C. B., & Pringle, J. E. 1994, *MNRAS*, 268, 1010
- Meliani, Z., Casse, F., & Sauty, C. 2006, *A&A*, 460, 1
- Mignone, A., Bodo, G., Massaglia, S., Matsakos, T., Tesileanu, O., Zanni, C., & Ferrari, A. 2007, *ApJS*, 170, 228
- Murphy, G. C., Ferreira, J., & Zanni, C. 2010, *A&A*, 512, A82+
- Parkin, E. R. & Bicknell, G. V. 2013, *ApJ*, 763, 99
- Pelletier, G. & Pudritz, R. E. 1992, *ApJ*, 394, 117
- Pudritz, R. E. & Norman, C. A. 1983, *ApJ*, 274, 677
- Pudritz, R. E., Ouyed, R., Fendt, C., & Brandenburg, A. 2007, *Protostars and Planets V*, 277
- Sauty, C. & Tsinganos, K. 1994, *A&A*, 287, 893
- Shakura, N. I. & Sunyaev, R. A. 1973, *A&A*, 24, 337
- Sheikhnezami, S., Fendt, C., Porth, O., Vaidya, B., & Ghanbari, J. 2012, *ApJ*, 757, 65
- Simon, J. B., Beckwith, K., & Armitage, P. J. 2012, *MNRAS*, 422, 2685
- Stone, J. M., Hawley, J. F., Gammie, C. F., & Balbus, S. A. 1996, *ApJ*, 463, 656
- Tzeferacos, P., Ferrari, A., Mignone, A., Zanni, C., Bodo, G., & Massaglia, S. 2009, *MNRAS*, 400, 820
- . 2013, *MNRAS*, 428, 3151
- Zanni, C., Ferrari, A., Rosner, R., Bodo, G., & Massaglia, S. 2007, *A&A*, 469, 811